Analysis of 5.5 years of atmospheric CO_2, CH_4, CO continuous observations (2014–2020) and their correlations, at the Observatoire de Haute Provence, a station of the ICOS-France national greenhouse gases observation network

Ludovic Lelandais, Irène Xueref-Remy, Aurelie Riandet, Pierre-Eric Blanc, Alexandre Armengaud, Sonia Oppo, Christophe Yohia, Michel Ramonet, Marc Delmotte

Atmospheric Environment 277 (2022) 119020

Contents lists available at ScienceDirect

Atmospheric Environment

journal homepage: www.elsevier.com/locate/atmosenv

Analysis of 5.5 years of atmospheric CO_2, CH_4, CO continuous observations (2014–2020) and their correlations, at the Observatoire de Haute Provence, a station of the ICOS-France national greenhouse gases observation network

L. Lelandais [a,*], I. Xueref-Remy [a], A. Riandet [a], P.E. Blanc [b], A. Armengaud [c], S. Oppo [c], C. Yohia [d], M. Ramonet [e], M. Delmotte [e]

[a] Aix Marseille Univ, CNRS, Avignon Université, Institut de Recherche pour le Développement IRD, Institut Méditerranéen de la Biodiversité et d'Ecologie marine et continentale IMBE, Technopôle Arbois-Méditerranée Bât, Villemin – BP 80, F-13545, Aix-en-Provence, cedex 04, France
[b] OHP Observatoire de Haute Provence, UMS Pytheas, CNRS, Saint-Michel-l'Observatoire, France
[c] Atmosud, Regional Agency for Air Quality monitoring, Marseille, France
[d] Aix Marseille Univ, Université de Toulon, CNRS, IRD, OSU Institut Pythéas, 13288, Marseille, France
[e] LSCE Laboratoire des Sciences du Climat et de l'Environnement, University of Versailles-Saint-Quentin-en-Yvelines, Gif-sur-Yvette, France

HIGHLIGHTS

- First study of atmospheric CO_2, CH_4 and CO time series in southern France.
- CO_2 and CH_4 annual growth rate congruent with north hemisphere annual growth rates.
- 30% of the 6.5 years time series are impacted by anthropic emissions.
- Enhancement ratios for winter anthropic impact reflect traffic and heating emissions.
- Biogenic sink and sources highlighted with vertical gradient between 100 and 10 m.

ARTICLE INFO

Keywords:
Atmospheric greenhouse gases
Enhancement ratio
South France
Observations
ICOS

ABSTRACT

Since 2014, a 100 m tall tower measures continuously greenhouse gases at the Observatoire de haute Provence (OHP) located in the southeast of France (43° 55′ 51″ N, 5° 42′ 48″ E) as a monitoring station of the French National Greenhouse Gases Observation network (ICOS-Fr). This rural station allows to study the short, mid, and long terms variability of atmospheric CO_2, CH_4 and CO concentrations at the continental, regional and local scales in a region characterized by a Mediterranean climate. Measurements are performed using cavity ring-down spectroscopy at three levels above ground level (AGL); 10 m, 50 m and 100 m. Using the ICOS European Infrastructure procedure to calibrate and ensure the data quality control, the precision of our datasets matches the international WMO/GAW recommendations. Time series from July 2014 to February 2020 were analysed. We inferred a mean annual growth rate at 100 m AGL of 2.7 ppm/year for CO_2 (7.8 ppb/year for CH_4) over the period of study, whereas no significant annual growth rate was found for CO. These growth rates are comparable to other remote ICOS and WMO/GAW sites. A seasonal amplitude of 13 ppm, 30 ppb, 45 ppb was found for atmospheric CO_2, CH_4 and CO, respectively. As expected, the amplitude of the diurnal cycle of these three species varies in function of the season, from 2.6 (1.6) ppm in winter and 10.7 (6.6) ppm in summer for CO_2, 3.7 (5.1) and 7.7 (7.1) ppb for CH_4, and contrary to CO2 and CH_4 smaller amplitude in summer with 2.15 (2.5) ppb and 9.3 (8.9) ppb in winter for CO at 10 m (100 m) AGL. Significant correlations (R^2 between 0.67 and 0.91) between the three species have been detected, especially in the winter season. Using thresholds on wind speed and on the standard variation of hourly concentrations, more than 16% of the data were identified to be enriched either: 1/ by regional anthropogenic plumes; 2/during stable synoptic conditions inducing the accumulation of anthropogenic emissions in the atmospheric boundary layer (13%); and 3/by local's sources inducing short pollution

* Corresponding author.
E-mail address: Ludovic.lelandais@imbe.fr (L. Lelandais).

https://doi.org/10.1016/j.atmosenv.2022.119020
Received 10 October 2021; Received in revised form 31 January 2022; Accepted 17 February 2022
Available online 2 March 2022

events (3%). On average, ΔCO/Δ CO_2 ratios of 3.72 ± 0.06 ppb/ppm and 0.8 ± 0.2 ppb/ppm for Δ CH_4/ΔCO were inferred during local pollution events in winter and are typical of traffic and residential heating as given by the local bottom-up emissions inventory delivered by the regional air quality agency ATMOSUD. Adding specific tracers or isotopic measurements would be very interesting to distinguish anthropogenic sources and monitor the evolution of their characteristics as emission ratios at the OHP station. Filtering out these conditions, about 84% of the data are not undergoing the influence of local and regional anthropogenic plumes, and are thus representative of "background" CO_2, CO and CH_4 concentrations at the local to the regional scales. These background conditions are shown to be dependent on wind speed and direction.

1. Introduction

The additional greenhouses gases (GHGs) emitted in the atmosphere since the industrial revolution by anthropogenic activities is causing severe changes on the earth radiative balance (IPCC 5th 2014). Major perturbations on the Environment and on the Earth, Climate occur at the global to the local scales (IPCC 5th 2014), and they represent one of the current major scientific and politic concerns. Since the Paris Agreement (United Nation Climate Change, 2015), 191 parties have legally committed to reduce their national GHGs emissions. To succeed they must quantify their emissions at the national scale. However, the variability of GHGs sources and sinks outcoming from the response of natural ecosystems to GHGs increase and from anthropogenic emissions (Wu et al., 2015; Xia et al., 2020) make it crucial to better characterize these signals at the regional scale to create efficient policies at the national scale.

Explicit regional budget of GHGs from inversion models based on atmospheric transport model and inventories (Saeki et al., 2013, Houweling et al., 2015) can be very useful (Broquet et al., 2013; Kountouris et al., 2018) for political decision. However, these models have several uncertainties due to inherent inventories incertitude (Rayner et al., 2010, McKain et al., 2012; Fischer et al., 2017; Hu et al., 2018) and a lack of direct observations to calibrate and validate models. Comparisons to direct observations are essential to assess the quality of the inversion (Chevallier et al., 2010; Bergamaschi et al., 2018). In addition, some biases persist in models such as topography which influence the mixing ratio, and atmospheric transport which induces sometimes large uncertainties (Geels et al., 2007).

Thanks to growing political concerns, scientific knowledge and technological improvements, the number of continuous monitoring stations to study GHGs has been increasing quite rapidly in the last decades. More than 100 stations are now gathered within networks under the umbrella of the World Meteorological Organization's (WMO) Global Atmosphere Watch (GAW) program (Schultz et al., 2015). Remote stations located in high altitude or far from sources and sinks such as in Mauna Loa, Hawaï (Keeling, 1960), Junfgraujoch, Switzerland (Uglietti et al., 2011) and Aigüestortes, Spain (Curcoll et al., 2019) are dedicated to studying continental to global trends and long-term atmospheric GHG variability but not local and regional ones. Until recently, the comparison from a site with a local to regional footprint to a remote station considered as a continental background (i.e., without the influence of local and regional anthropogenic emissions) was performed to isolate the contribution of local and regional GHGs fluxes to atmospheric GHGs concentrations monitored at the local/regional site (Schmidt et al., 2003; Vogel et al., 2010; Lopez et al., 2013; Xueref-Remy et al., 2018). However, the remote continental stations are often too far from the local/regional ones, inducing biases due to additional emissions interacting with the atmosphere during the transect of the air mass to the station (Ammoura et al., 2015; Schmidt et al., 2014). Airborne measurements are an effective way to record regional signal (Xueref-Remy et al., 2011) but the cost and the dependency to clear weather conditions still limit airborne measurements (Abshire et al., 2013). Similarly, the precision of GHGs observations from space is still not enough sufficient (Kort et al., 2012; Ye et al., 2020) to match with the World Meteorological Organization (WMO) Global Atmosphere Watch (GAW) ±0.1 ppm for carbon dioxide in the Northern WMO-CO_2-X2019 (Hall et al., 2020), and ±2 ppb for methane WMO-2004). To be able to monitor local and regional GHG signals, tall towers equipped at different levels appear to be an appropriate tool (Bakwin et al., 1998; Haszpra et al., 2001; Stavert et al., 2019). According to Gloor and al 2001, a 500 m tall tower has a spatial footprint of 10^6 km^2 or more. In Europe, the Integrated Carbon Observation System (ICOS) network, operational since 2012 (https://www.icos-ri.eu/), is designed to establish a dense network of regional and local scale stations for the monitoring of atmospheric greenhouse gases, mainly carbon dioxide (CO_2), methane (CH_4), and for some stations nitrous oxide (N_2O) and carbon monoxide (CO), a tracer used to discriminate natural GHG fluxes and emissions outcoming from combustion processes. It contains twenty-seven tall towers and results from some of these towers are published by Vermeulen et al., (2011), Schmidt et al., (2014), Conil et al., (2019) for example. Countries participating to the ICOS European Infrastructure also have complementary stations on their national ground. This is the case of France, which owns the ICOS-France network equipped with 12 stations, among which only 4 belong to the ICOS European network. ICOS-France is a homogeneous network made of one standardized instrumentation, a unique calibration and drift control strategy, as well as homogeneous data treatment and quality control procedures performed within the ICOS database, as described in Hazan et al. (2016) and Conil et al. (2019). The ICOS and ICOS-France stations are dimensioned to meet the WMO/GAW objectives mentioned above.

Our study focuses on the OHP ICOS-France station located in the South-East of France (SUD-PACA region) at the Observatoire de Haute Provence (43° 55′ 51″ N, 5° 42′ 48″ E). According to IPCC 5th (2014), the SUD-PACA region is much exposed to the risks of climate change, which include perturbations of the carbon cycle at the local to the regional scales. The tower, operational since July 2014, has 3 levels of measurements (10 m, 50 m and 100 m AGL) for monitoring continuously atmospheric CO_2, CH_4 and CO. The tower is also equipped at the same levels with meteorological sensors. The site is also monitoring fine particles with a diameter smaller than 2.5 μm and 10 μm (PM2.5, PM10), ozone (O_3) and water vapor (H_2O) thanks to regional air quality agency ATMOSUD but will not be described in this study.

In this study, after a description of the site location, of the meteorological conditions and of the instrumental set ups, we analyse the variability of atmospheric CO_2 and CH_4 from July 2014 to February 2020, exploring correlations between CO_2 CH_4 and CO at different spatial and time scales (diurnal, synoptic, seasonal and interannual ones). We then assess the anthropogenic impact of local to synoptic sources on the station. From these results, we conclude on the most appropriate criterion to define when the ICOS-France OHP station is representative of the regional background CO_2 and CH_4 signal i.e., with no influence of local and regional sources.

2. Materials and method

2.1. Site description

The ICOS-France OHP station (43° 55′ 51″ N, 5° 42′ 48″ E, 650 m a.s.l.) is composed of a 100 m height tower and is located in the SUD PACA region, southeast of France (Fig. 1 a), at the Observatoire de haute

provence. This region covers 31 400 km^2 i.e., 5.7% of the national territory. In 2015 almost 70% of the region were covered by forest and natural areas, and the population was 5 million habitants. Urbanized and industrialized areas represent 8.2% of the land use (DREAL PACA).

The tower is fully dedicated to atmospheric observations and equipped at three levels for continuous measurements at 10 m, 50 m and 100 m AGL where CO_2, CH_4, CO and water vapor are monitored. In addition, meteorological instruments are installed at the same levels in order to record temperature, atmospheric pressure, relative humidity and wind speed and direction. Air is continuously sucked by the instrumentation located at the bottom of the tower in a 22° ± 0.1 °C temperature-controlled container.

The tower near neighbourhood (<2 km) is a pubescent oak forest (Quercus pubescents) with a small village Saint Michel l'Observatoire with about thousand inhabitants located at 3 km at the south of the Tower (Fig. 1c). The nearest city is Forcalquier with five thousand inhabitants located at 4 km at the northeast of the OHP station (Fig. 1c). The major city is Manosque (21 thousand habitants) located at 12 km at the South-east of the tower (Fig. 1c). It concentrates many industrial activities and represent about 107 kt CO_2 emitted in 2017 (https://cigale.atmosud.org). A major highway passes through Manosque and is located from 20 km at the northeast and 20 km at the south of the station. The Aix -Marseille metropolis is located at about 80 km at the south (Fig. 1b). The Rhone valley which concentrates many manufactures, industrials sites and major cities as Avignon (with about a hundred thousand inhabitants) and smaller (with about thirty thousand inhabitants) as Cavaillon and Carpentras are located at 70 km at the west of the OHP (Fig. 1b). Belviso et al., (2016) shows that industrials carbonyl sulfide emissions from this region could reach OHP and impacted the station. The Aix – Marseille metropolis is located 80 km south of OHP (Fig. 1b) and represents the most important anthropogenic area in the region. This metropolis is the second biggest one of France, with about 1.8 million habitants. Its emissions (20 Mt CO2 in 2017 https://cigale.atmosud.org) are estimated to represent 7% of the national CO2 emissions (CITEPA inventories 2019 https://www.citepa.org/fr/secten/) and close to half of the regional emissions (ATMOSUD, https://cigale.atmosud.org). Finally, Lyon the third biggest French city with about half million inhabitants is located at about 200 km at the northwest of the OHP (Fig. 1b).

Thanks to the high-resolved (1 × 1 km2, 1 h) regional emissions inventory from ATMOSUD (https://cigale.atmosud.org), we can identify the main sectors of activity that contribute to emit atmospheric CO_2, CH_4, CO, PM10 and PM2.5, here given for 2017. For the Aix-Marseille metropolis area, four sectors are the main contributor of CO2 and CO emissions: the industrial sector represents 56% of CO_2 emissions (and for CO 62%), the traffic with 16% (7%) and the residential with 6% (and 16%) and energy production with 14% (6%). These sectors are also responsible of 60% of PM10 and PM2.5 emissions. CH_4 is emitted by other sectors of activity: 78% of CH_4 are estimated to outcome from waste treatment and 5% from the agricultural sector (ATMOSUD, https://cigale.atmosud.org).

2.2. Meteorological fields

In this section, we describe the main meteorological patterns at OHP derived from the hourly ICOS-fr datasets at 10 m, 50 m and 100 m AGL on the period of study (07/07/2014–02/29/2020).

Regarding synoptic wind patterns, the mean speed is 2.7 ms^{-1}, 3.6 ms^{-1} and 4.9 ms^{-1} at 10, 50 and 100 m AGL at these elevations, the first quartile (25%) is 1.4 ms^{-1}, 2 ms^{-1} and 2.2 ms^{-1}, respectively and the third quartile (75%) is 3.7 ms^{-1}, 6.3 ms^{-1} and 7 ms^{-1}, respectively. The dominant wind sector is the North-West one (NW), which represents 20% of the data on the three levels (Fig. 1). About half of wind measured at 100 m AGL from the NW have a mean hourly speed higher than 8 ms^{-1} and a maximum speed of 28 ms^{-1}. This dominant wind is endemic of the region and is called 'mistral'; it is created by the corridor made by the Alps on the East side and the Massif Central on the other side. Another regional wind called 'tramontane', formed by the gap between the Massif Central/and the Pyrenees (precisely described in Drobinsky and al 2005 and Jiang Q. and al 2003), is often associated with the mistral because they blow in a similar direction with relatively speed higher than 7/8 ms^{-1} (Drobinsky et al, l 2005). Furthermore, mainly at 50 m and 100 m, winds coming from the NE sector represent between 10% and 15% of the data with a maximal frequency during winter.

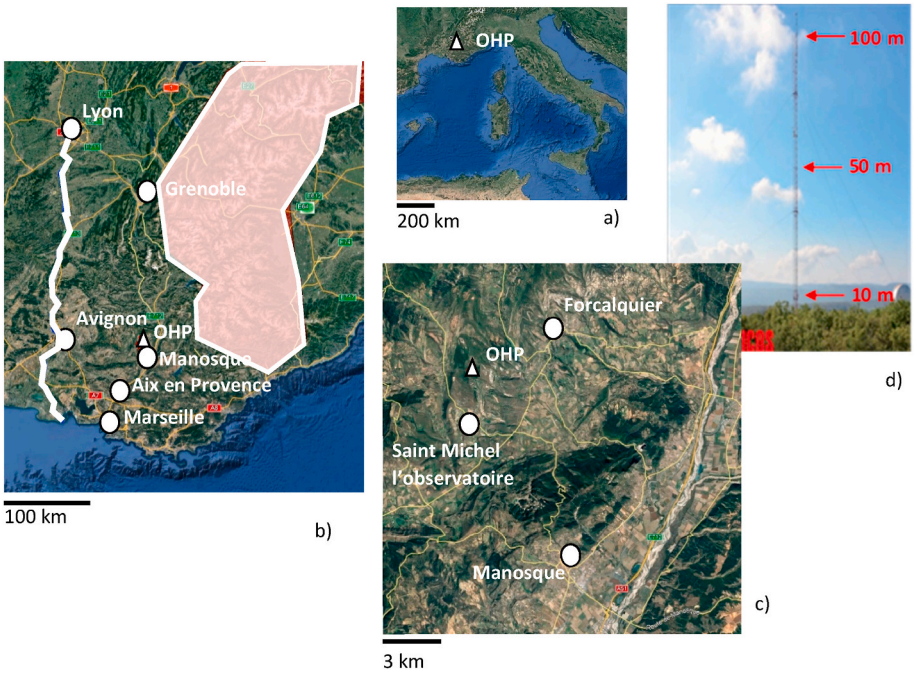

Fig. 1. (colors not required). Photography of OHP tower (d) and 3 satellite pictures (from google earth) illustrating the landscape and location of OHP and main cities at 3 scales (a,b,c). The white area in b) represent Alps mountains and white segment represent Rhone valley. (For interpretation of the references to color in this figure legend, the reader is referred to the Web version of this article.)

Besides, the area is characterized by local wind patterns. The land/sea breezes process occurs in the southern part of the SUD-PACA region, due to its proximity to the Mediterranean Sea (Delbarre et al., 2005). Within the ESCOMPTE campaign organised in the Marseille area, it was demonstrated that sea breezes can penetrate in land several tens of kilometres from the coast (e.g., Bastin and Drobinski, 2006; Drobinski et al., 2006) but it has not been deeply investigated at the coordinates of OHP. At this site, during summer the South-west (SW) sector becomes more important and represents 15% of the total winds for the three levels (Fig. 2). More specifically, between 12h00 and 16h00, south-southwest sector represents more than 40% of wind at the three level (as illustrated in S.1).

The region benefits from a Mediterranean climate with hot dry period during summer and a mild, wet winter. Over the period of study, the temperature ranged from a minimum monthly mean of 2.1 °C in winter at 10 m (February 2018) and maximum of 25 °C (July 2019) in summer. The summer (winter) mean is about 22 ± 2 °C (6 ± 2 °C). Precipitations are not monitored at the station, but relative humidity provides information about the water amount in the atmosphere. The minimal relative humidity monthly mean is during August 2017 with 46.5% and the highest is in November 2018 with 80%. The summer mean is about 56 ± 6% and the winter mean is 67 ± 6% at 10 m AGL. Temperature means are equal at 10 m and 100 m AGL and relative humidity mean difference between 10 and 100 m AGL is close to 3–5%.

In order to characterize the origin of the air masses arriving at OHP, we calculated backward trajectories using the Hysplit Lagragian model (Draxler et al., 1997). For this study, the model relies on NCEP reanalysis (with a daily mean resolution and 2.5-degree latitude x 2.5-degree longitude global grid (144 × 73)) from the National oceanic and atmospheric administration and the National Center for environmental prediction (NOAA). Seasonal mean backward trajectories were calculated for summer (June, July, and August) and winter (December, January, and February) at 100 m AGL. between 2014 and 2019 every 6 h over 96 h total, then aggregated in order to calculated frequencies showed in Fig. 3.

Hysplit calculation showed northwest as the dominant sector representing about 50% of total arrival air mass (Fig. 3). The geographical origin of the other half depends on the season and of synoptic conditions. In Summer, about 30% of the air masses arrived from the South according to Hysplit and about 21% from the northeast. In winter the other half of winds come from east sector for 30% and west for 20%. Hysplit calculation appeared congruent with wind Rose regarding the dominance of the northwest sector, an impact of the sea in summer with wind coming from south uniquely in summer and the presence of winds from northeast sector arriving at the OHP. Whereas difference and accuracy in the repartition sectors remain between Hysplit reanalysis and Wind roses from observed data due to the large resolution grid (2.5°).

2.3. Instrumentation and calibration procedure

The CO_2, CO and CH_4 datasets were collected at a 0.2 Hz frequency and averaged every minute between 07/07/2014 and 02/29/2020 using a cavity ring down spectroscopy analyzer (CRDS) Picarro (G2401 model) at 10, 50 and 100 m (AGL). Each level is sampled for 20 min, alternatively. Due to a technical issue, the data at 50 m (AGL) are valid since January 29, 2015 only. Each level is sampled through a Synflex pipe (4.3 mm diameter). The automatic ICOS control procedure applies a time correction to take account of the time spend by the air in the volume of the air line (close to 10 L for the 100 m line) between the time of the sampling and the time of the measurement in the CRDS analyzer cavity, which represent a correction of about 1.65 min. The cavity temperature of the PICARRO analyser is controlled and maintain at 45 °C (T0) and the pressure at 140 Torr (P0). In order to protect the cavity of the analyzer, each airline is equipped with a filter (M&C TechGroup) to remove particles larger than 2 μm before air enters the instrument.

The calibration and drift control of the instrument are performed automatically through a rotationnary valve using 6 cylinders qualified on the international World Meteorological Organization (WMO) scales for atmospheric CO_2, CO and CH_4 following the ICOS procedures (Hazan et al., 2016), alternatively with air measurements. These procedures are explained in detail in Conil et al. (2019).

Each night, the datasets are transferred to the ICOS database and then processed according to the ICOS automatic data treatment and quality routines Hazan et al. (2016). Mostly, all data points with $|P- P0| > 0.1$ Torr and $|T -T0| > 0.004$ °C are excluded. Furthermore, dead volumes in the setup led to instability in the response of the analyser for less than 5 min after switching from one gas line to another. These 5 min

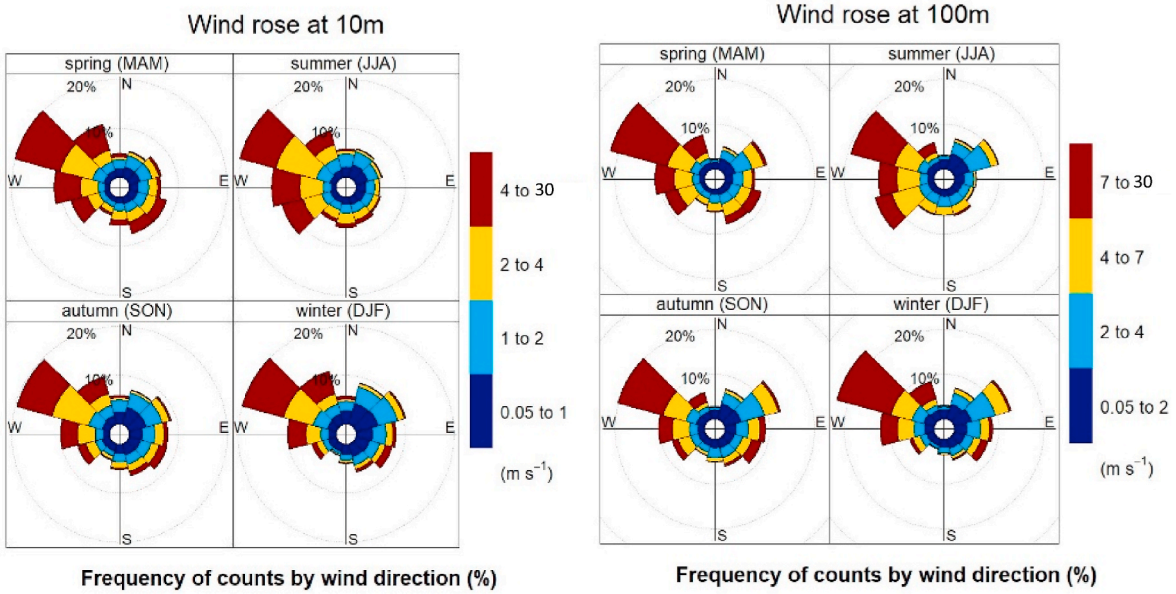

Fig. 2. (colors required). Windrose at OHP at 10 m AGL (left panel) and 100 m AGL (right panel) given by season over the period study (from November 26, 2014 to February 29, 2020). The colors indicate the wind speed values according to the given scale (in ms^{-1}). (For interpretation of the references to color in this figure legend, the reader is referred to the Web version of this article.)

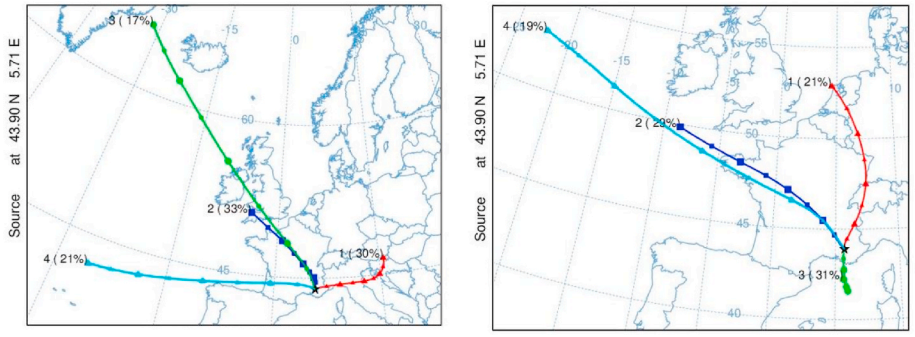

Fig. 3. (colors not required). 96 h mean back trajectories (and associated frequencies) reaching OHP (100 m AGL) over the period of study in winter (left) and in summer (right) from the HYSPLIT model and NCEP data reanalysis (Daily mean resolution with 2.5-degree grid). (For interpretation of the references to color in this figure legend, the reader is referred to the Web version of this article.)

periods were automatically removed from the datasets. To correct for the superimposition of the species absorption bands monitored in the 1.6 mm wavelength range, a water vapor correction provided by PICARRO is automatically applied on the datasets (Hazan et al., 2016). Finally, the datasets are manually inspected on a regular manner by the station P.I. and flagged for any anomalies (leaks, human respiration during routine operations on the tower …).

The precision and accuracy of the instrument over the period study respect ICOS recommendations reported in Laurent, 2017 Table 3 and fit the WMO GAW compatibility goals perform for CO_2 and CH_4. According to Camille Yver 2015 the precision and the repeatability for the continuous measurements repeatability and the long term repeatability measurements were calculated. Over period of study the repeatability and the precision are 0.1 (0.02) ppm for CO_2; 0.23 and 0.26 ppb for CH_4 and 4.96 and 0.52 ppb for CO.

In the following study, we use hourly means. Time is given in UTC. Local time at OHP correspond to UTC+2 from April to October and UTC+1 from November to March.

2.4. Boundary layer height simulation

The atmospheric boundary layer height was simulated using the WRF-ARW model (Skamarock, 2004) forced by ECMWF meteorological fields (ERA reanalysis) at a 2 × 2 km2 and 1 h resolution, on a domain covering about 50 km north of OHP to the bay of Marseille and the east coast of Spain to the east coast of Corsica. Due to some technical and human ressources limitations, we could product a dataset covering the period from 02/11/2015 to 06/05/2019, without the month of January 2018. These data are used to assess the diurnal and seasonal variability of the atmospheric boundary layer height at OHP.

3. Results and discussion

3.1. Timeseries overview

The hourly average concentrations of atmospheric CO_2, CH_4, CO collected at 10 m, 50 m and 100 m (AGL) measured at 4 m (AGL) from 07/07/2014 to 02/29/2020 are presented in Fig. 4. For the three species at 10 m and 100 m (AGL). The number of valid minute data over the study period for 10 m and 100 m (AGL) ranges between 480 000 and 490 000 for the three species, representing about 42 000 hourly means. At 50 m (AGL), about 450 000 min data are valid, representing about 36 000 hourly means. The exact numbers of data available for each species and level are listed in Supplementary Material S.2.

CO_2, CH_4, CO, concentrations reveal an important seasonal pattern. 95% of CO2 is between 393.1 and 423.5 ppm. CH_4 annual range is close to 100 ppb between 1860 and 1960 ppb. CO_2 and CH_4 pattern have maximal values reached in winter and minimal reached in summer contrary to CO which have low value in winter and high in summer.

All the species presents numerous short periods with high concentrations. During these periods, concentration peaks are often three times higher than the mean monthly variability (defined as the mean standard deviation of hourly averages for each month) and five time higher for CO. CO highest peaks reach 220 ppb whereas the mean monthly variability is close to 20 ppb. CH_4 and CO_2 highest peaks exceed about 4 times the monthly variability (22 ppb and 4 ppm respectively). The variability of the different species at different time scales and in function of wind conditions is analysed further below.

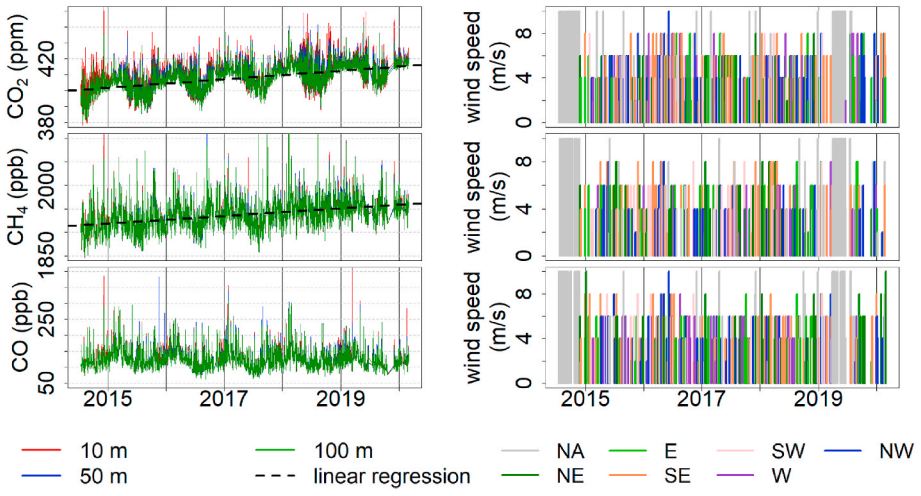

Fig. 4. (colors required). Timeseries of atmospheric CO_2, CH_4, CO hourly measurements at 100 m (green), 50 m (blue) and 10 m (red) (AGL) and of atmospheric From July 2014 to February 2020 except for data from 50 m which start in January 2015. Bars at the right represents synoptics events occurrence, size of the bars represents winds speed categories associated (<2, 2–4, 4–8, >8 ms^{-1}) and each colour represent the main wind sector of an event. (For interpretation of the references to color in this figure legend, the reader is referred to the Web version of this article.)

3.2. Annual growth rates

The annual growth rate of CO_2 and CH_4 was studied before analysing their shorter variations at the seasonal and diurnal scales. The annual growth rate is crucial to monitor average trends of long lifetime species on periods larger than one or more decades. In this study, we analysed the evolution of the annual growth rate of these species over 5 years, and not their trend due to the relative short length of the record (<10 years).

Firstly, to limit the influence of local emissions, only data collected at 100 m AGL were selected. Then, to remove highly polluted data, the Standard deviation method explained by El Yazidi et al., (2018) was applied on the minute data: this first step removed from 2.3 to 3.9% of the data depending on the species and on the measurement's height. Next, the data were hourly averaged and for each hour, the first and third quartiles were calculated. All the data comprised between these two quartiles were retained (Vermeulen et al., 2011). These data were aggregated by day, and then a sliding mean (Roustand et al. 2008) of 365 days was calculated to reduce the impact of seasonal variations. Finally, a linear regression was applied to these datasets to determine the mean annual growth rate, as the coefficient slope of the fit. As in Vermeulen et al., (2011), several filters were tested: (1) taking the lowest hourly daytime mean per day, (2) selecting only the first quartile (25% lowest) of each hour, (3) choosing the data comprised between the 1st and the 3rd quartiles for each hour, and (4) applying the Theilsen function which calculate the robust Sen-Theil slope estimator (Sen, 2021) available with R package OpenAir (Carslaw et al., 2012). The results obtained with these four different methods are reported in Table 1. The proximity of the tower to potential important biogenic sinks of CO_2 in summer conducted us to the hypothesis that choosing method (1) or the (2) would create a bias related to the interannual variability of biospheric fluxes. As Vermeulen et al., 2011 method (3) based on the selection of the data between the first and the third quartiles was kept limiting the impact of potential strong sources and sinks.

An increase of +2.7 ppm/year is determined. This is concordant with the 2.6 ± 0.09 ppm/year mean growth rate provided by NOAA for the northern hemisphere between 2015 and 2019 (https://www.esrl.noaa.gov/gmd/ccgg/trends/gl_gr.html) but a little bit higher than the annual growth rate found at other ICOS sites, e.g. at Cabauw in Holland with 2 ppm/year between 2005 and 2009 (Vermeulen et al., 2011) and at Observatoire pérenne de l'environnement (OPE) station in the East of France with +2.5 ppm/year between 2011 and 2018 (Conil et al., 2019). The mean growth rate over our period study is little higher than those found in these other studies (Vermeulen et al., 2011; Conil et al., 2019) likely because of the important impact of strong growth years rate 2015 and 2016 coupled with the small number of years. Moreover, the site variability is also explained by geographical differences. Cabauw and OPE station have a temperate oceanic climate with less extreme season contrary to OHP station which has a Mediterranean climat characterize partly by hot and dry summers (Beck et al. 2018). Extreme drought influencing CO_2 emissions by modifying plant response and global carbon cycle (Ramonet et al. 2017; Rodenbeck al 2020; Smith et al., 2020). Besides, as show in Ramonet et al. 2017, interannual variability of atmospheric boundary layer impact the emission footprint of stations. Shalow atmospheric boundary layer height increases footprint of emission on the station, at the OHP, atmospheric boundary layer height observation is not yet available, but it will be interesting in future study to investigate atmospheric boundary layer variability.

Over the period of study, the annual growth rate was very different from one year to the other (Table 2). Due to the short record in 2014 (6 months) and in 2020 (2 months), the annual growth rate of these two years was not calculated individually. In 2016, the CO_2 annual growth rate was +3.68 ppm/years at OHP, which is much stronger than the mean rate observed between 2015 and 2019 on our site. This highest value could be explained by two mechanisms: first, stronger anthropogenic emissions (Cigale inventory, ATMOSUD). In 2016, CO_2 (CH_4) regional anthropogenic emissions were 2.5% (20%) and 1.5% (3%) higher than in 2015 and 2017. Second, an El Niño event occurred in the Winter 2015–2016 (NOAA and Ivakhov and al 2019) and induce increase in CO_2 growth rate (Betts RA. et al., 2018). El Niño events are positively correlated with an increase of the global CO_2 growth rate (Patra et al., 2005, Wang W. and al 2013): for example, an uplift of 1 ppm of the annual mean CO_2 global timeseries was found resulting from El Niño 1983 (Gaudry et al., 1987). However, a similar annual growth rate is observed at OHP in 2019, while the El Niño event in 2018–2019 was weaker by far than event in 2015/2016. Regional emissions inventories were not available yet for this year, but one explanation could be the high temperature levels encountered during the Summer 2019. It was the hottest summer of the period of study according to the literature (Oldenborgh et al., 2019, Vautard et al., 2020, https://climate.copernicus.eu/record-breakingtemperatures-june). Unfortunately, meteorological instruments did not record from April 08, 2019 to July 30, 2019 so we cannot compare at the OHP precisely. However, GV Van Oldeborgh et al. 2019 record a highest temperature of two degree compared to the highest values in 1981–2010 in France and explain it by the amplification of the soil moisture drying which amplified temperatures means and extremes. Previous studies showed heat waves induced higher marine and terrestrial CO_2 emissions which can also partially explain this high rate (e.g., Ramonet et al. 2017, Arias-Ortiz et al., 2018; Gerdol et al., 2008; Ramonet et al., 2020; Smith et al., 2020). Interranual variability of CO_2 growth rate is possibly influenced by interranual variability of meteorological condition, of atmospheric dynamics (as the atmospheric boundary layer height) and annual anthropic emissions.

Over the period of study, the mean CH_4 annual growth rate is 7.85 ± 1.3 ppb/year with a maximal value in 2016 (+12 ppb/year) and a minimum value in 2017 (+3.3 ppb/year). The mean rate at OHP is close to the NOAA global CH_4 growth rate of +8.2 ± 0.6 ppb/year over the same period (Dlugokencky and Tans, 2020; https://www.esrl.noaa.gov/gmd/ccgg/trends_ch4/). Turner et al. 2016 "demonstrate that the problem of attributing methane trends from the current surface observation network, including isotopes, is underdetermined and does not allow unambiguous attribution of decadal trends" this increase can be explained by several factors. Causes of the recent rise since 2007 of atmospheric methane remain not fully understood (Nisbet et al. 2019; Turner et al., 2019) several hypotheses are currently debating in atmospheric community. On one hand a decrease in the oxidation power of the atmosphere due to a decrease of the OH radical which is the main

Table 2
Annual growth rate of CO_2, CH_4 for each year between 2015 and 2019 at OHP.

Year	CO_2 (ppm/year)	CH_4 (ppb/year)
2015	2.2	7.2
2016	3.7	12.2
2017	2.4	3.3
2018	2.2	9.6
2019	3.8	6.3

Table 1
Mean annual growth rate over 2015–2019 of atmospheric CO_2, CH_4 and CO calculated with the 4 methods explained in the text.

	(1) Minimal hourly mean per day	(2) Data <25%	(3) Data between 1st and 3rd quartile	4) Theilsen
CO_2 (ppm)	2.7	2.80	2.7	2.5
CH_4 (ppb)	8.2	7.8	7.9	7.2
CO (ppb)	−1.3	−1.9	−2.0	−2.3

Table 3
Coefficient of determination (R^2) between pairs of species measured at 10 m (AGL) in function of wind sector (60° each) and windspeed classification during Winter (December, January, February).

Wind speed: 0 - 2 ms^{-1}							
Wind sector	N-NE	E	SE-S	S-SW	W	NW-N	All directions
(CH_4, - CO_2)	0,748	0720	0,719	0689	0,770	0770	0,734
(CO, CO_2)	0,686	0696	0,678	0649	0,709	0714	0,685
(CH_4, CO)	0,817	0835	0,829	0809	0,826	0810	0,822
Wind speed: 2 - 4 ms^{-1}							
Wind sector	N-NE	E	SE-S	S-SW	W	NW-N	All directions
(CH_4, CO_2)	0,739	0731	0,794	0729	0,775	0827	0,774
(CO, CO_2)	0,713	0719	0,749	0672	0,723	0826	0,724
(CH_4, CO)	0,761	0800	0,808	0802	0,822	0848	0,808
Wind speed: >4 ms^{-1}							
Wind sector	N-NE	E	SE-S	S-SW	W	NW-N	All directions
(CH_4, CO_2)	0,911	0871	0,840	0727	0,733	0837	0,808
(CO, CO_2)	0,914	0878	0,767	0551	0,755	0841	0,804
(CH_4, CO)	0,880	0928	0,802	0778	0,806	0826	0,822

sink of atmospheric CH_4 (Kirschke et al., 2013, Turner et al., 2017) could induced a weaker sink and so the rise of atmospheric CH_4 (Turner et al., 2017; Rigby et al., 2017). On the other hand, an increase of emissions can also explain this rise. It is important to note that simultaneously to the CH_4 rise, a decrease in global $\delta\ ^{13}C_{CH4}$ is observed. Schaefer et al., (2016) support that an increase of microbial emissions from wetlands and livestock which have strong negative isotopic ratios could explain the actual trend of rising CH_4 and decreasing $\delta\ ^{13}C_{CH4}$. Controversially, an increase of emissions from natural gases supported by a rise of ethane of 2.3 [1.8, 2.8] x 10^{-2} ppb yr^{-1} since 2007, a tracer for oil and gas emissions (Hausmann et al., 2016), could also explain the CH_4 rise, but not the isotopic ratio decrease. To explain both trends with a rise of emission from natural gas, a concurrent decrease of a rich ^{13}C source must occurred. Worden et al., in 2017 suggest that the strong rich ^{13}C source concurrent decrease could be biomass burning and fire emissions. It is possible that both changes are indeed occurring. Both microbial and fossil fuel emissions could increase and still explain the isotopic signature decrease and CH_4 increase if microbial isotopic fluxes are higher enough than fossil fuel fluxes or if biomass burning emission are decreasing too. In the PACA region, ATMOSUD inventories found that yearly anthropic CH_4 emissions in the SUD PACA region varies between 2015 and 2018 of about 18%, with maximal amount of CH_4 emit in 2017, which surprisingly correspond to the lower CH_4 annual growth rate (3.3 ppb/year) we found over the period (Table 2). Besides, Nisbet et al. 2019 found for populated North area from 30° to 50° that the CH_4 growth "was not led by fossil fuel emissions" which is congruent with the absence of relation observed between the CH_4 annual growth rate and the ATMOSUD inventories. However, Nisbet et al. 2019 found some noticeable episode of growth in 2014 and 2016 with annual growth rate close to 10 ppb which is congruent with our 2016 annual growth rate of 12.2 ppb. They explained these important annual growth rate by annual air temperature warmer but the temperature variation do not match the CH4 annual growth rate. Despite the absence of clear temperature effect to explain 2016 high annual growth rate, Turner et al., (2019) found that ENSO event mostly contributes to the not long-term variability impacting the OH variability which could be part of explanation for the strong annual growth rate founded in 2016. The lowest annual growth rate of 3.3 ppb found in 2017 remain unexplained. Moreover, as CO_2 annual growth rate variability, the atmospheric dynamics (as the atmospheric boundary layer height variability) should be one of the factors responsible of this strong interannual variability by changing the footprint of emission on the station.

Despite the short lifetime of CO compared to CH_4 and CO_2, we also applied the same method on the CO record of OHP and we obtained a mean rate of – 2 ppb/year over 2015–2019. Despite the low significance of the regression ($R^2 = 0.25$), this decrease seems congruent with recent observations in the North Hemisphere (Lowry et al., 2016) resulting of strict emission policies. A longer timeseries of CO measurements at OHP should permit to detect more robustly the regional decrease of atmospheric CO.

3.3. Seasonal cycles

The seasonal cycle of atmospheric CO_2, CH_4, CO, is presented on Fig. 5. Minute data were aggregated at the hourly scale and then averaged by month. The growth rate of CO_2 and CH_4 was removed from the datasets at the three sampling levels before calculating the means.

As expected (Stanley et al., 2018; Conil et al., 2019), CO_2, CH_4 and CO show higher concentrations in the cold months, and lower concentrations during Summer. The seasonal amplitude of the CO_2 concentration is about 13 ppm with a maximal monthly average of 409.3 ± 2.2 ppm measured at 10 m (AGL) in February and a minimal of 396.5 ± 2.4 ppm in August. These variations are partially explained by the atmospheric boundary layer height (ABLh) seasonality which induces a stronger dilution of emitted sources from the surface in Summer than in Winter (560 m AGL on average during summer and 267 m AGL in winter (cf. Fig. 5). Over the period of study, April has the smallest mean standard deviation with 0.7 ppm while October has the largest one, close to 2.7 ppm. More extreme values are found close to the surface in comparison with the top of the tower because of the higher proximity to sources and sinks. The amplitude of the CO_2 vertical gradient $\Delta V_{[sp]}$ ($\Delta V_{[sp]} = [sp]_{100m}\text{-}[sp]_{10m}$ (AGL)) is smaller in winter than in summer and is maximal in May and June (as illustrated in Fig S.4). During summer, a strong negative vertical gradient is found with a difference of 5 ppm ±0.1 between 100 m (AGL) and 10 m (AGL) due to high CO_2 emissions by plant respiration and the shallow nocturnal boundary layer which is in average lower than 200 m during the night (cf. Fig. 6). In opposite, during daytime in summer, a positive vertical gradient is found with a CO_2 value about 1 ppm ±0.1 lower at the bottom than at the top induced by the CO_2 uptake by the photosynthesis sink despite a larger atmospheric boundary layer that reaches 1200–1400 m (cf. Fig. 6). These cyclic variations result from the cumulative effects of the seasonality of the biospheric activity, which induce a local sink of atmospheric CO_2 during spring and summer and a source in winter (Nasrallah et al., 2003; Miller et al., 2020) and the seasonality of the ABLh, that is higher in Summer than in Winter as it is shown in Figs. 5 and 6 and congruent with literature (Medeiros et al., 2005; Koffi et al., 2016; Gu et al., 2020).

The CH_4 seasonal cycle shows an amplitude of about 30 ppb. The maximum occurs in February (1926 ± 12.6 ppb) and the minimum in August (1892.8 ± 10.6 ppb). Similar shape of the CH_4 seasonal cycle is observed in other sites of Europe (Schmidt 2014; Vermeulen et al., 2011; Popa et al., 2010; Fernández-Duque et al., 2017). The minimal concentrations encountered in summertime are caused by photochemical reactions of methane molecules with hydroxyl radicals (Fernández-Duque et al., 2017). The vertical gradient $\Delta V_{[sp]}$ ($\Delta V_{[sp]} = [CH_4]_{100m}\text{-}[CH_4]_{10m}$ (AGL)) between 10 m and 100 m (illustrated in Fig S.4) is higher in early winter and close to zero between May and August. Natural CH_4 emissions are higher in winter and autumn in the northern hemisphere and the CH_4 seasonal cycle is directly related to the rate of hydroxyl radical production, which depends on photochemical processes (IPCC 5th 2014). Moreover, according to ATMOSUD inventories, in the vicinity of OHP (~15 km around the OHP), there are three main emission sectors of CH_4: animal farming representing about 41% of total emissions, compacted landfill about 38% and residential heating for 15%. Residential heating appears as be the only one with a significant seasonal variation explaining partially higher concentration in winter due to higher emissions coupled as CO_2 concentration to a lower

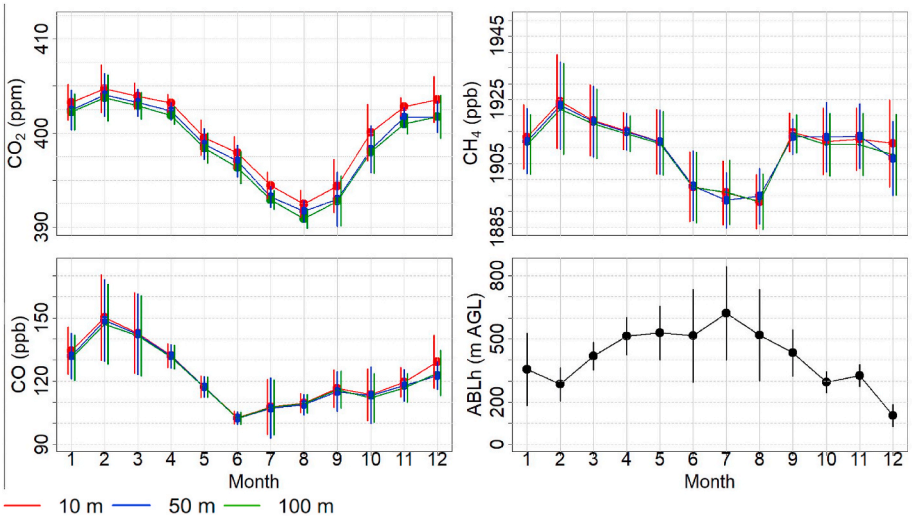

Fig. 5. (colors required). Seasonal cycles of CO_2, CH_4, CO at 100 m, 50 m and 10 m and of the atmospheric boundary layer height (ABLh) from our WRF-ECMWF modelling framework. Altitudes are given AGL. The 10 m and 100 m datasets run from 07/07/2014 to 02/29/2020, and the dataset collected at 50 m starts on January 29, 2015. The ABLh dataset covers the period from 02/11/2015 to 06/05/2019 (without January 2018). The bars represent 1-σ of the means. (For interpretation of the references to color in this figure legend, the reader is referred to the Web version of this article.)

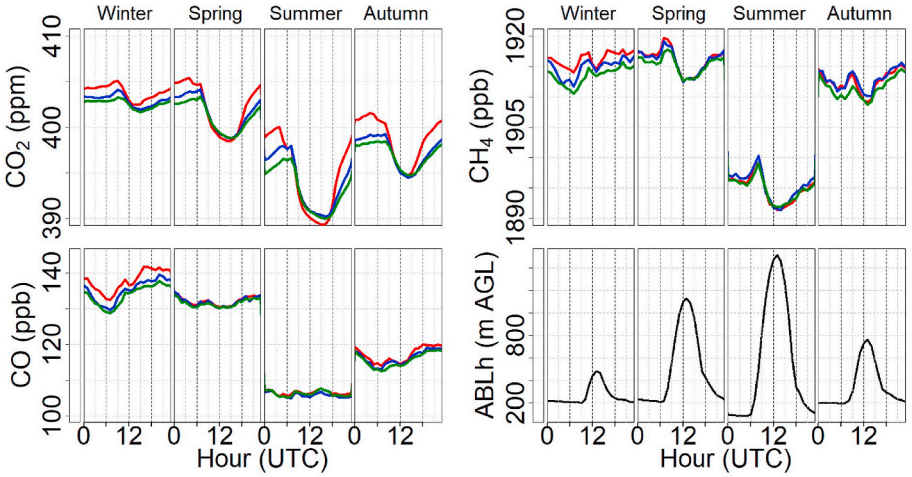

Fig. 6. (colors required). Diurnal cycle of atmospheric CO_2, CH_4 and CO at OHP at 100 m (green), 50 m (blue) and 10 m (red) and modelized atmospheric boundary layer height (ABLh) from our WRF-ECMWF modelling framework. The data are averaged from 07/07/2014 to 02/29/2020, except for the data collected at 50 m which start on January 29, 2015. Altitude is given AGL. The dataset for the ABLh covers the period from 02/11/2015 to 06/05/2019 (except January 2018). (For interpretation of the references to color in this figure legend, the reader is referred to the Web version of this article.)

atmospheric boundary layer height (cf. Fig. 5).

The CO seasonal cycle has higher values during winter, especially in February and March, with monthly mean concentrations exceeding 150 ppb. This can be attributed to higher anthropogenic emissions and a smaller atmospheric boundary layer in wintertime (cf. Fig. 5.). The lowest monthly mean concentrations occur in June and July (~105 ppb). The CO vertical gradient is the strongest in early Winter, with a maximum difference of 10 ppm ±0.5. No gradient is observed between April and September. As for CH_4, the CO seasonality is (1) directly linked to the seasonality of his main sink, which is the radical OH: the concentration of this latter depends on sun light and is thus higher in summer than in wintertime; and (2) also controlled by the seasonality of the atmospheric boundary layer height.

3.4. Diurnal cycles

As for the seasonal cycle, the diurnal cycle of the different species studied here is mainly driven by atmospheric dynamics and biospheric activities but also by human emissions. These factors have different impacts depending on species.

A CO_2 diurnal cycle is observed at each sampling level of the ICOS-Fr OHP tower. Its amplitude is higher at 10 m AGL than above, especially in Spring and Summer. Its amplitude depends on the season and varies from 6.0 ± 3.7 ppm in wintertime to 15.9 ± 6.6 ppm in summertime at 10 m AGL. CO_2 mean hourly concentrations are higher in night-time than during daytime, because CO_2 emitted by anthropogenic activities and biosphere respiration accumulates into a smaller atmospheric boundary layer (Schmidt et al., 2014). The mean standard deviation of CO_2 is close to 4 ppm (Figure S.3). In winter biogenic CO_2 fluxes from soils are still important and is directly linked with sol temperature (Fang et al., 2016; Doukalianou et al., 2019) if soil temperature stands above 0 °C. At OHP, air temperature remains mainly above 0 °C even in winter: thus, soil respiration could play an important role on the CO_2 diurnal cycle, even in Winter. As illustrated on Fig. 6, in wintertime the boundary layer height is close to 200 m (AGL) during the night. In the morning, the development of the atmospheric boundary layer (ABL) occurs with sunrise i.e. at 06h00 in Summer and 09h00 UTC in Winter and brings CO_2 at 50 m and 100 m: this explains the maximum occurring after 09h00 UTC at these levels, visible in winter. CO_2 hourly mean concentrations are the smallest between 12h00 and 18h00 UTC, due to a high well mixed ABL, and photosynthesis activity of local vegetation.

As for CO_2 and CH_4, the CO concentration starts to increase at 07h00 UTC and stops at 11h00 UTC in Winter and 09h00 in Autumn. The CO concentration increases during afternoon (13h00 – 16h00 UTC) close to the surface. The mean interannual variability of the CO diurnal cycle at 10 m (AGL) (100 m (AGL)) is 25.1 ± 1.5 ppb (23.5 ± 1.3 ppb). The diurnal evolution of the CO vertical gradient during Winter is well correlated with the diurnal cycle of the atmospheric boundary layer height, as already described in the literature (Liu et Lang 2010; Xiang et al., 2019). As for CO_2 and CH_4, higher value close to the surface reflect

non negligible sources from human activities (Popa et al., 2010).

At last, in winter and for wind speed lower than 2 ms^{-1}, even after subtracting annual growth rate on CO_2 and CH_4 datasets the diurnal cycle of each species shows some interannual shift as it is illustrated in Fig. 7. The same interannual variability is visible at 100 m (AGL), and only for low wind speed as for the 10 m AGL level. The winter 2019–2020 presents the lowest CO_2 diurnal cycle (402.3 ± 1.1 ppm) contrary to 2017–2018 winter when the mean is 406.3 ± 1.5 ppm with a shift of 4 ppm. For the compared years, the shift for CO diurnal cycle is about 25 ppb and 11 ppb for CH_4 diurnal cycle. Except for the 2015–2016 Winter, which is associated to the lowest CH_4 diurnal cycle, and the 2014–2015 one which is related to atypical and high diurnal cycles for the three species, the CO_2, CO and CH_4 diurnal cycles vary similarly and appeared well correlated with the diurnal cycle of air temperature. One of promising factor influencing this interannual variability of diurnal cycle could be the variability of the atmospheric boundary layer height which is directly linked with the air temperature. Cold years are associated with relative higher diurnal cycle which could be explained by a higher concentration of species in a smaller boundary layer. Indeed, the hottest Winter seasons of our study (2015–2016 and 2019–2020) are associated with the lowest CO and CO_2 diurnal values, and as the opposite, the Winter 2017–2018 is the coolest and the corresponding diurnal cycles are associated with some of the highest values of CO_2 and CO. Local winter emissions are not available for the years of the study and only for 2013, but according to the literature, CO_2 emissions (especially heating) are directly correlated with air temperature and low temperatures reduce the combustion efficiency of engines and increase their CO emissions by a factor 5 to 6 (e.g. Ward et al., 2015; Liu et al., 2012 and Andrews et al., 2004). Carbon isotopic measurements in CO_2, also associated to CO_2 flux measurements, would be interesting to quantify the role of the biogenic and anthropogenic sources. Nevertheless, the analysis of the ratios between CO_2, CO and CH_4 presented in the next section already helps to assess the role of anthropogenic emissions at different spatial scales in Winter.

3.5. Anthropogenic impact on the OHP station

3.5.1. CO_2, CO and CH_4 correlations

In this section, we investigated the influence of anthropogenic emissions on the timeseries collected at OHP, from the local to the regional (synoptic) scale. We classified the CO_2, CO and CH_4 concentrations in 24 groups according to six wind sectors of 60° each and 4 speed classes (low: 0–2, medium: 2–4, strong: 4–8, and mistral >8 ms^{-1}). Only Winter data were selected, to maximize the impact of emissions. For each group, we be studied the correlation between CO_2, CO and CH_4 using a Spearman correlation test provide by the "stats" R package.

The results are given in Table 2. The three species seem well correlated regardless of the wind sector ($R^2 > 0.67$). For strong windspeeds (>8 ms^{-1}), R^2 was high (>0.8) between the 3 pairs of species but number of data by wind sectors was low so we choose for correlation table to not put them in the table due to the lack of data by sector. For low wind speeds, R^2 is every time higher between CH_4 and CO than between CH_4 and CO_2 and between CO and CO_2. The coefficient of determinations with CO_2 are the lowest of all values given in Table 2: this may be explained by the small biospheric activity persisting during wintertime. The significative correlation between the pairs of species in winter are mainly due to a low ABL height (Fig. 6), weak sunlight inducing reduced photochemical sinks for CO and CH_4, low biospheric activities inducing a reduced source and sink of CO_2 and higher anthropogenic emissions in that season (Xueref Remy et al., 2018; Conil et al., 2019). As a precaution, we also calculated the coefficients of determination between the pairs of atmospheric species for the summer period: congruent with former studies (e.g., Satar et al., 2016; Conil et al., 2019) we found no strong correlation between the three species in summertime. During the warm period, drivers and emissions are different than in the cold months, as the natural biospheric contribution controls much more the CO_2 concentration than in Winter. Despite, we found a certain correlation in Summer for wind speed <4 ms^{-1} between CO and CH_4 ($R^2 \sim 0.5$), which could originate from their common photochemical sink in Summer.

In order to quantify the impact of local to regional anthropogenic emissions on atmospheric CO_2, CO and CH_4 at OHP, we defined impacted hours as every hour showing a concentration higher than one standard deviation added to the median diurnal cycle of each month averaged over the entire period of study. Indeed, we tried several methods to define a proper threshold, using the mean diurnal cycle, or moving windows. It appears than the definition that we retained is the best trade-off to detect short events of a few hours and long events of several days, as it keeps any linear relationship existing between different species. An illustration of the results obtained with the different methods tested is available in Supplementary Material S.5.

Using the selected method, our analysis shows that between July 2014 and February 2020, for each species and for each sampling level of

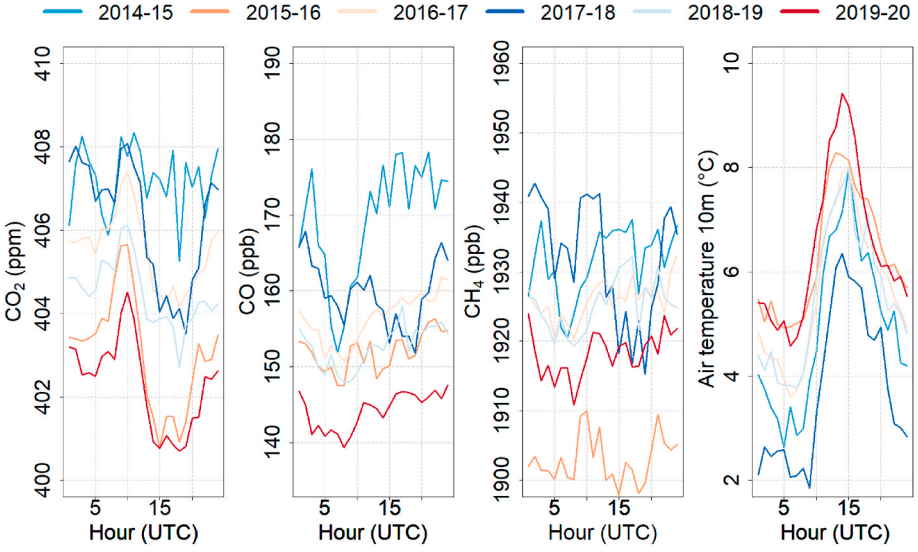

Fig. 7. (colors required). Winter diurnal cycle of CO_2, CO and CH_4 for low winds speeds and global air temperature diurnal cycle at 10 m (AGL). (For interpretation of the references to color in this figure legend, the reader is referred to the Web version of this article.)

the OHP ICOS tower (10 m, 50 m and 100 m AGL), the number of impacted hours represents between 14% and 20% of the total dataset (cf. Table 5).

3.5.2. Impact of synoptic events

Here, we assessed how regional anthropogenic emissions influence the OHP station by being transported as an anthropogenic plume to the site through synoptic meteorological conditions and lasting a few hours to a few days. We consider a "period" of the timeseries as being "impacted" by such a plume if at least 3 consecutive hours of the data are higher than the threshold defines in Section 3.5.1. We consider as the same event two consecutives "impacted period" if the delay between those was lower than 6 h, to consider atmospheric boundary layer dynamics. By performing this analysis on the CO_2, CO, CH_4 hourly timeseries for the whole period of study, we detected between 347 and 523 independent events regarding the species and the level of measurements of the OHP ICOS tower. The median duration of these events ranges between 7 h for CO_2 and 11 h for CH_4 (Table 5). Table 4 gives descriptive statistics on these events for each species and each level. The strongest event (illustrated in Supplementary material S.6) recorded for CO_2, CH_4 and Co-occurred early December 2014 and lasted three days from 6 to 8 December with a maximal (mean) increase of concentration recorded at 100 m (AGL), reaching 31,8 (21.2) ppm, 142.7 (101.4) ppb and 165.3 (110.7) ppb above the median of the monthly diurnal cycle. Plotting 96 h back trajectories from the Hysplit model, we found that the air mass came from the Grenoble area, which is highly urbanized and industrialized. We assumed that the relatively lower number of anthropogenic synoptic events detected at 50 m for CO_2, CO and CH_4 are due to the 6 months shorter time series available at 50 m (see Section 2.3).

At 10 m (AGL), almost every event has mean wind speed lower than 4 ms^{-1} Impacted hours at 10 m (AGL) with slow winds represent 80% of the total (see Fig. 8). Slow winds have already been identified as a main factor explaining high concentrations of greenhouse gases (Idso et al., 2002, Xueref-Remy et al., 2018). Most of these events are encountered during night-time or/and wintertime (see Fig. 8). The small and stable boundary layer height occurring in Winter and at night is described in many studies (Fujitani et al., 1986, Koffi et al., 2016; Liu et al., 2020; Bakas et al., 2020) and is favourable to greenhouse gases and pollutants accumulation (e.g., Xueref-Remy et al., 2018; Xiang et al., 2019) close to the surface. Small values of the boundary layer height at night and during wintertime at OHP is comforted by WRF model outputs of this parameter (see Fig. 6). Based on windspeed, we can assume that events at 10 m (AGL) are mainly due to stable meteorological conditions inducing surface accumulation speed lower than 4 ms^{-1} represent 80% of the events at 10 m (AGL) and about 50% of event recorded a 100 m (AGL) (see Fig. 8). The other half at 100 m (AGL) corresponds to windspeeds higher than 4 ms^{-1} (see Fig. 8) and may indicate arrivals of polluted air masses from dense urbanized and/or industrialized areas. Although no significative pattern appears on CO_2, CO and CH_4 impacted hours along the day.

The distribution of the synoptic anthropogenic events by wind sector is given in Supplementary material S.7a. The West sector (240–300°) is associated with the highest number of events (more than 25% for all species). The West and North-West sectors correspond to the Rhone Valley, which is highly industrialized, and that has already been demonstrated to be a source of atmospheric pollutants for OHP (Belviso et al., 2016). The South-West sector (180–240°), which includes the Aix-Marseille-Provence metropolis represents less than 10% of all events for CO_2 and CH_4 at the three ICOS tower levels (Supplementary material S.7 b). This could be explained by the wind distribution pattern at OHP, where winds from the South-West sector are the less occurrent. Back trajectories computed from the HYSPLIT model for several events showed arrivals of air masses at OHP during synoptic events from several urbanized/industrialized areas such as Avignon, Lyon, Grenoble, and Aix Marseille metropolis. As an example, Fig. 9 show a synoptic event that occurred from October 14, 2020 to October 17, 2020 which brought high concentrations of CO_2, CO, to OHP from the Aix-Marseille-Provence metropolis area. During this event CO_2 at 100 m (AGL) was in average (maximum) higher of 3.3 ± 4.6 ppm (14.6) than the monthly mean diurnal cycle, CH_4 was higher by 59.6 ± 26.2 (97.9) ppb and CO was higher by 49,9 ± 30.4 (96.9) ppb.

Table 5
Descriptive statistics on the locally short-term impacted hours of the datasets collected at 10 m AGL for CO_2, CH_4 and CO.

Species (at 10 m AGL)	CO_2	CH_4	CO
Number of hours	1293	684	870
% Of selected data with our method	3.1	1.6	2.1
% Of selected data with El Yazidi method	2.6	2.6	3.8
Median mean amplitude (ppm for CO_2/ppb for CO and CH_4)	5	25.3	23.2
Highest mean amplitude (ppm for CO_2/ppb for CO and CH_4)	32.4	362.6	202.9

3.5.3. Impact of local emissions

Finally, to identify the impact of punctual local emissions such as traffic peaks on atmospheric CO_2, CO and CH_4 concentrations at OHP, we focused on isolated impacted hours recorded close to the ground at 10 m (AGL), for wind speed lower than 2 ms^{-1}. We excluded hours associated with synoptics events to avoid long term mixing. This selection based on wind speed and duration of high concentration allowed us to reduce the footprint of the data within a radius of 20 km, and to avoid long term transport i.e., longer than 3 h. As an independent estimate of our results, we also applied another selection method on the datasets, described in El Yazidi et al., (2018) and based on the standard deviation of the data over a moving window of one week. On ours CO_2 CH_4 CO datasets at 10 m (AGL) the mean standard deviation over one week is 1.7 ppb, 6.54 ppb and 5.92 ppb respectively. Both methods gave consistent results, which lead to the estimation that less than 5% of data are impacted by local sources. The main statistics of these data are summarized in Table 5.

The North-East, East, and South-East sectors represent 71% of the local impacted hours. Along daytime, we notice that the locally impacted hours show specific patterns regarding the predominant wind sector (illustrated for CO on Fig. 10). Impacted hours associated with winds from the North occur mainly during night-time and could be reflecting the accumulation of residential emissions in the shallow nocturnal stable boundary layer. Whereas locally impacted hours associated to winds blowing from East and South-East are more frequent the morning and the early afternoon (7 h–14 h UTC) and could be related to

Table 4
Descriptive statistics of the anthropogenic synoptic events for CO_2, CH_4 CO at the three levels of the OHP ICOS tower. Amplitudes are given in ppm for CO_2 and in ppb for the other species.

Species (Alt AGL)	CO_2 10 m	CO_2 50 m	CO_2 100 m	CH_4 10 m	CH_4 50 m	CH_4 100 m	CO 10 m	CO 50 m	CO 100 m
Number of events	523	448	510	379	347	377	422	395	423
% Of data	14.83	12.45	14.79	15.87	13.54	15.51	17.29	14.80	17.11
Median duration (h)	7	7	7	11	10	11	10	10	10
Maximal duration (h)	91	83	93	100	90	108	116	92	168
Median of all average amplitude (ppm/ppb)	4.70	4.37	4.07	24.48	24.44	24.14	25.09	24.21	23.53
highest average amplitude (ppm/ppb)	25.15	14.55	19.59	116.52	97.75	111.58	128.41	79.34	113.60

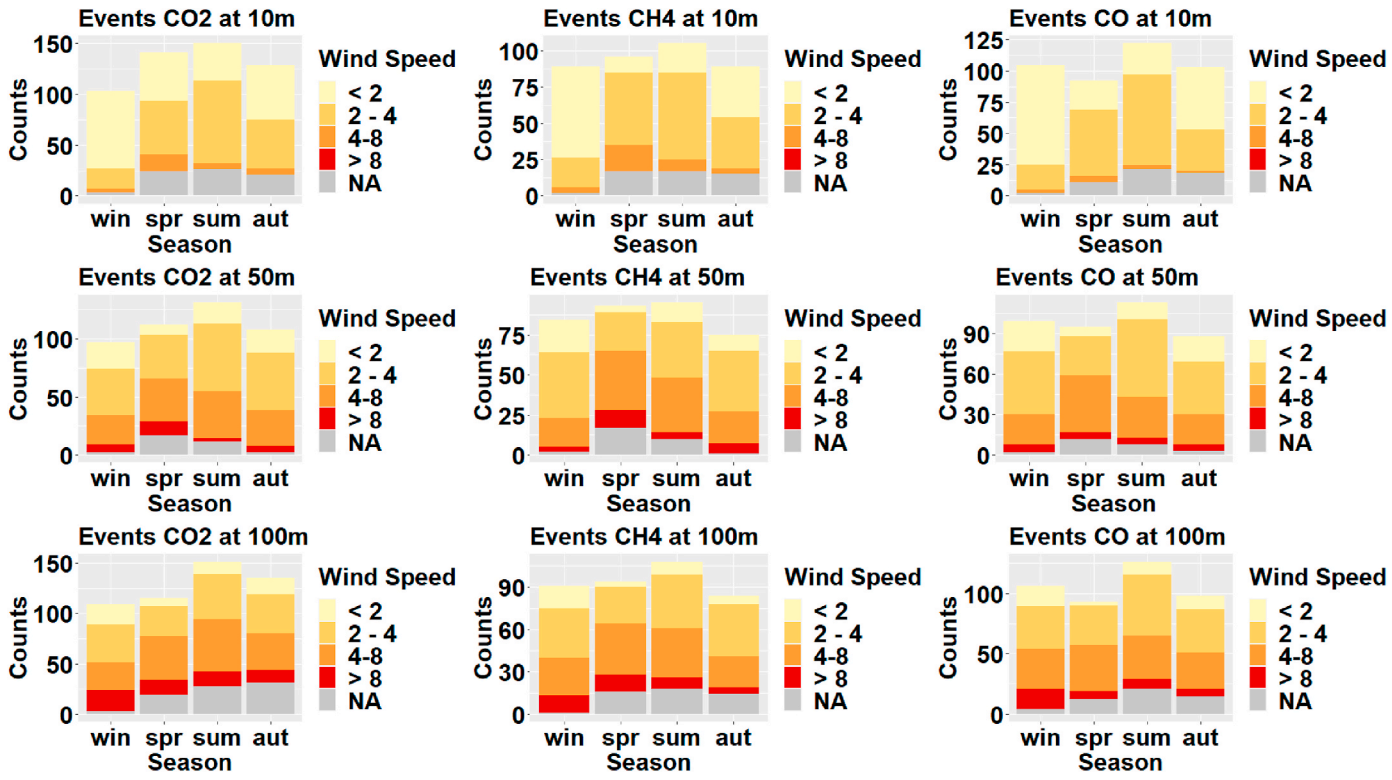

Fig. 8. (colors required). Synoptics events of CO_2, CH_4 and CO (at 10 m, 50 m and 100 m AGL) distributed by season and wind speed in m/s. (For interpretation of the references to color in this figure legend, the reader is referred to the Web version of this article.)

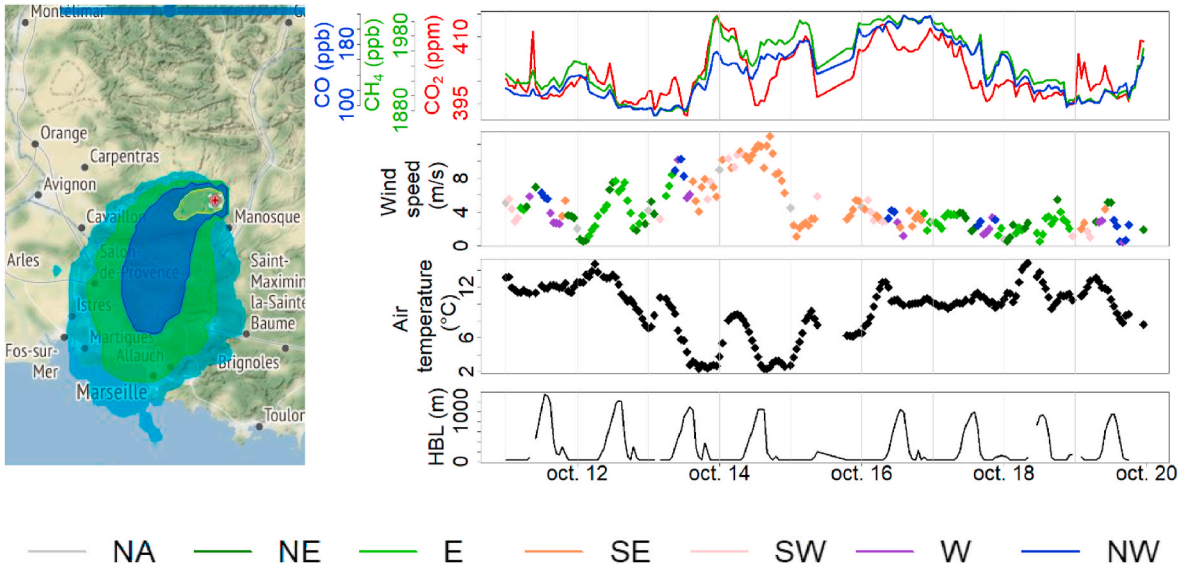

Fig. 9. (colors required). Left: Atmospheric CO_2 (red), CH_4 (green) and CO (blue) concentrations at 100 m (AGL), during a synoptic event observed on October 14, 2015 at OHP. Right: 48 h back dispersion plume from the HYSPLIT model using winds from GDAS archive at a resolution of 0.5° and 3 h resolution, starting on 15 October at 18 h UTC. (For interpretation of the references to color in this figure legend, the reader is referred to the Web version of this article.)

emissions from traffic on the A51 highway and from several cities, such as Manosque located ~15 km further in the South-East. The variability of locally impacted hours of fine Particulate Matter with daily wind patterns follow the one described previously for CO_2, CH_4 and CO. This similar behaviour indicates that CO_2, CO and CH_4 impacted hours are rather due to anthropic emissions as traffic or residential heating, which are also associated with PM emissions (Liu et al., 2020), than to biospheric fluxes.

The calculation of the ratios between the enhancements called Δ of two different species X and Y above the thresholds defined above can help identifying the sources of emissions (e.g., Xueref-Remy et al., 2011; Popa et al., 2014; Ammoura et al., 2016) which impact locally the hourly concentrations. We thus calculated the different combinations of ΔX/ΔY ratios between CO_2, CO and CH_4 for each hour. Using a scatterplot, we use a linear fit applied to a ΔY vs ΔX plot. ΔX (respectively ΔY) is defined as the X (resp. Y) locally impacted hour concentration minus the corresponding hourly mean value of the monthly median cycle. The slope of the line represents the so-called "enhancement ratio".

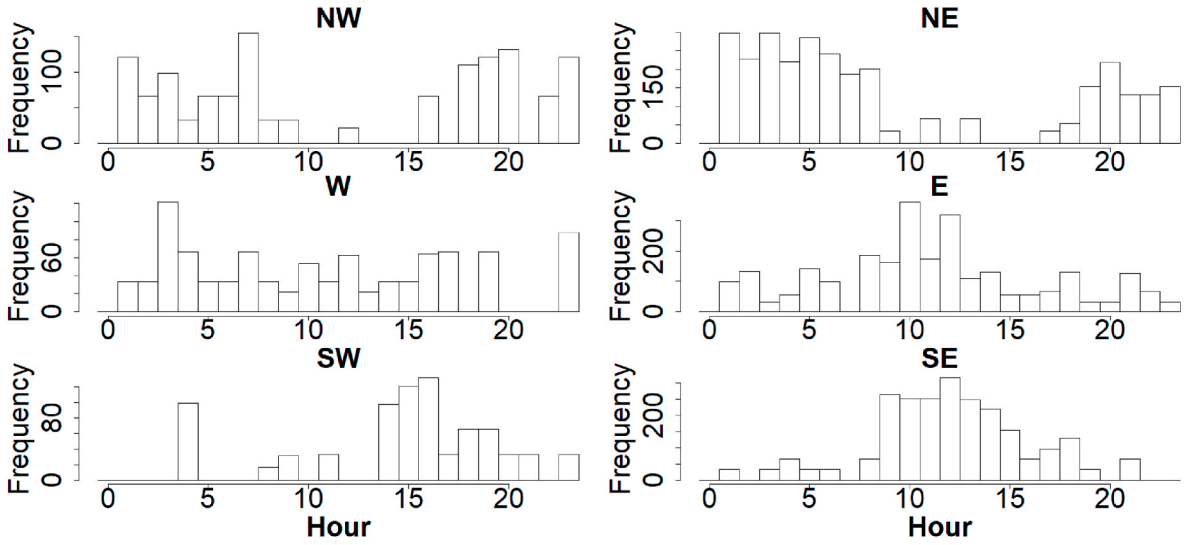

Fig. 10. (color not required). Density of locally impacted hours of CO, recorded at 10 m AGL on the OHP ICOS tower, and corresponding to wind speed lower than 2 ms^{-1}, in function of daytime and by wind sector.

We chose to focus minute data when ΔX and ΔY were correlated with a R^2 coefficient greater than 0.5 and a P value less than 0.05 for the entire hour. The results are given in Table 6 according to the different wind sectors.

In the next paragraph observed ratio form literature and OHP station are given with a 1/1000 mass fraction ratio: ppb/ppm for Δ CO/Δ CO_2 and Δ CH_4/Δ CO_2, in ppb/ppb for Δ CO/Δ CH_4, these are directly comparable with SECTEN and ATMOSUD Inventories which give emissions in kg for the three species and are reported in Table 7. We found a positive correlation between ΔCO (ppb) and Δ CO_2 (ppm) with a mean ratio of 3.72 ± 0.06, ranging from 3.23 ± 0.16 to 4.37 ± 0.11. These values are consistent with the ones given in the literature. In studies dedicated to traffic, a Δ CO/Δ CO_2 ratio of 5.6+-2.43 (8.4 ± 0.45) was determined from observations for fluent (congested) traffic in Paris, France (L. Ammoura et al., 2014) and a Δ CO/Δ CO_2 ratio of 4.15 ± 0.34 in Islisberg, Switzerland (Popa et al., 2014) for fluent traffic. Emission inventories estimate a similar range of CO/CO_2 ratio for traffic emissions: at the national level, the SECTEN 2017 inventory gives a CO/CO_2 ratio of 2.57, while at the regional scale, the ATMOSUD 2017 inventory provides a CO/CO_2 ratio of 2.43. For the year 2013, ATMOSUD provided an emissions inventory for the whole SUD-PACA region at a spatial resolution of 3 km for each month of the year. Using this inventory, we aggregated CO_2 and CO emissions in winter in a 40 km-side square centred on the OHP site. A mean CO/CO_2 ratio of 11.09 was calculated, which is much higher than the enhancement ratio observed at OHP. Indeed, the local ATMOSUD 2013 winter inventories provides CO/CO_2 ratios of 3.25 and 23.34 for domestic heating. At OHP, the mean ratio observed is 3.7. It indicates that local emissions impacting OHP are dominated by the traffic sector because we never observe a Δ CO/Δ CO_2 > 5. Whereas average emissions ratio for wintertime provided by the literature and by inventories are much higher (R.R. Buchholz et al., 2016: 8.26–25.2, Turnbull et al. 2015: 7, Bares et al., 2018: 7.38, local 2013 ATMOSUD inventory: 11.09). Residential heating emissions ratio provided by inventories are close to 24 (Local and regional ATMOSUD inventories and national SECTEN inventories). Whereas, regarding the temporal variation of this ratio, we observed lower ratios close to 2.8 during the night between 02h00

Table 6
OHP enhancement ratios Δ CO/Δ CO_2, Δ CO/Δ CH_4 and Δ CH_4/Δ CO_2 in winter at 10 m (AGL) for low wind speed using minute data (indicated in column 5) when the hour correlation between CO_2, CH_4 and CO two by two have a R^2 coefficient greater than 0.5 and a P value less than 0.05. Correlation with *** have a $R^2 \geq 0.8$; **$R^2 \geq 0.7$; *$R^2 \geq 0.5$.

Wind sector	Δ CO/Δ CO_2	Δ CH_4/Δ CO	Δ CH_4/Δ CO_2	Nb of minutes selected
NW	4,37 ± 0.11 ***	0.98 ± 0.04 **	3.62 ± 0.09 ***	814
NE	3,63 ± 0.17 *	0,58 ± 0.03 *	4.42 ± 0.14 **	1668
W	3,23 ± 0.16 **	1,06 ± 0.04 ***	2.79 ± 0.11 **	660
E	4,10 ± 0.15 **	0,77 ± 0.03 ***	3.96 ± 0.11 **	1086
SW	3.54 ± 0.21 **	0,86 ± 0.04 ***	3.41 ± 0.17 **	538
SE	3.32 ± 0.23	0,58 ± 0.04	3.97 ± 0.16 *	1421

Table 7
Enhancement ratio for CO_2, CO and CH_4 from inventories and literature for anthropogenic emissions. Δ CO/Δ CO_2 and Δ CH_4/Δ CO_2 ratio are à 1/1000 ratio whereas Δ CH_4/ΔCO is a 1/1 ratio.

	sector	Δ CO/Δ CO_2	Δ CH_4/Δ CO	Δ CH_4/Δ CO_2
Ammoura et al., 2014	traffic (fluent)	5,68 ± 2.43		
	traffic (congested)	8,44 ± 0.45		
Popa et al. (2014)	traffic	4,15 ± 0.34		
Buchholz et al., 2016	urban	8,26–25,2	2,2 - 13	19–61
Turnbull et al. 2015	urban	7		
Bares R et al., 2017	urban	7,38		
SECTEN 2017national	total	7,68	0,86	6,59
	domestic	25,63	0,12	3,07
	traffic	2,57	0,01	0,04
SECTEN 2013 national	total	8,77	0,73	6,43
	domestic	26,50	0,11	2,81
	traffic	3,55	0,01	0,05
ATMOSUD 2017 régional	total	5,86	0,47	2,77
	domestic	15,76	0,07	1,05
	traffic	2,43	0,01	0,04
ATMOSUD 2013 regional	total	5,92	0,40	2,37
	domestic	12,44	0,07	0,87
	traffic	4,00	0,01	0,05
ATMOSUD 2013 12 km around OHP	total	11,09	0,19	1,52
	domestic	24,14	0,05	1,18
	traffic	3,24	0,01	0,02

(UTC) and 04h00 (UTC) than during the day, which is characterized by ratios higher than 4.5. Assuming that local traffic close to the OHP is relatively low during the night, this value could illustrate an improvement of efficiency in heating devices, as it been described in the literature (Ammoura et al., 2016; Popa et al., 2014). Indeed, the CO/CO_2 enhancement ratio from traffic and domestic emissions has been decreasing since several years because of significant technological improvements in combustion efficiency. The higher global ratios provided by local inventories could be explained by an overestimation of local CO emissions related to heating emissions.

$\Delta CH_4/\Delta CO$ ratios inferred from the OHP timeseries range from 0.88 to 1.86. For wintertime, the ATMOSUD local inventory of 2013 provides a CH_4/CO ratio close to 0.19, which is lower than the ratios provided by the 2017 annual national inventory (SECTEN, 0.88) and regional inventory (ATMOSUD, 0.47).

Moreover, the $\Delta CH_4/\Delta CO_2$ ratio measured at OHP ranges between 2.7 and 4.42, with higher values when winds blow from the East. The 2013 ATMOSUD local inventory provides for wintertime a lower ratio of 1.51. By contrast, the ATMOSUD regional inventories for 2013 and 2017 provide an annual ratio of 2.3 and 2.7 respectively. The SECTEN national inventory delivered an annual $\Delta CH_4/\Delta CO_2$ ratio of 6.4 (6.6) for 2013 (2017). According to Lin et al., (2015) and references therein, $\Delta CH_4/\Delta CO$ ratio >0.3 in wintertime are in the range of ratios indicatives urban/industrial sources. There are too high to be explained by biomass/biofuel burning which is lower than 0.3 (Andreae and Merlet, 2001; Mühle et al., 2002) which indicates impact of fossil fuel emission. Furthermore, several studies (e.g., McKain et al., 2012; Boothroyd et al., 2018; Xueref Remy et al., 2020), demonstrated that leaks from natural gas storage sites and distribution networks can lead to important release of methane in atmosphere. At OHP, this CH_4 enrichment could be explained by an additional CH_4 emissions from a potential gas storage site located at 10 km from the station or from the close cities. Regarding wind rose pattern (Fig S. XX) a CO and CH_4 concentration at 10 m (AGL) are higher with CH_4 concentration reaching 1980 ppb and CO concentration close to 170 ppb when winds come from the Northeast. As we explained previously north is associated with residential emissions from heating. Lower ratio from local inventories could reflect an underestimation of CH_4 emissions from such missing sources and from residential heating. Regarding the emission categories listed in the ATMOSUD local inventory, we noticed that the gas storage and distribution one are not present.

Due to three level alternance measurements and quality process which does not consider five first minutes of each record, we only have 15 min per hour at 10 m, after the data selection on wind speed and correlation of the three species, we retain above 300 independents hours. This number is not enough to establish a significant variability of the ratios per hour, year, or winds sectors, and to clearly separate the influence of traffic emissions from residential heating ones or from other local sources at these spatio-temporal scales. Complement tracers or proxies and longer time series are needed to go further in this investigation with robust statistics. Black carbon data for tracing wood burning for residential heating, NOx measurements as a proxy of traffic, as well as carbon isotopes data to distinguish different combustion sources could provide the complement of information needed. Besides, emission estimates delivered by the inventory at the regional and national scales were available for the entire year and not for Winter, and the local inventory of 2017 were not available during this study; it would be interesting in the future to compare the observed ratios with the data from the 2017 local inventory, and, to compare them with the data from the regional and national inventories for winter only, whenever possible.

3.5.4. *Natural vs anthropogenic contributions at OHP*

Fig. 11 shows the timeseries before (red) and after (green) applying the filter defined in section 3.5.1 on the CO_2, CH_4 and CO data measured at 100 m (agl). Including all synoptic events and local emissions, the total contaminated hours represent about than 30% of the data. The differences between the filtered and the non-filtered timeseries range from 1 to 5 ppm for CO_2, and from 10 to 15 ppb for CH_4 and CO. These difference from filtered and non-filtered data represents above 1.25, 0.52 and 7.7% of CO_2, CH_4 and CO signals at the OHP station. This percentage varies with the wind direction (illustrated in Fig. S.9), the highest differences between the non-filtered and the filtered datasets being associated with West and North-West winds. As illustrated in Section 3.5.1, West and North-West sectors are related to numerous and strong synoptic events from the Rhône valley and Lyon/Grenoble areas and residential emission especially in winter, which explains a stronger anthropic impact from these sectors. The southwest sector is associated with strong emissions from the Aix-en-Povence city and the Berre lake industries (about 60–80 km), which are especially visible on the CO dataset during the afternoon and the evening (due to the time of traveling to OHP), inducing CO concentration higher of about 20 ppb (about 160 ppb in winter and 110–120 ppb in summer at 10 m AGL, cf. Fig S.10) compared to the average of CO recorded the afternoon and evening of each season (summer: 108.43 ± 20.1 ppb and winter: 141.2 ± 32.3 ppb). The CO_2 dataset does not show such increase of concentration, probably due to the biospheric sink induced by the vegetation surrounding OHP (cf Fig S.11). Concentrations of CH_4 close to 1900 ppb are

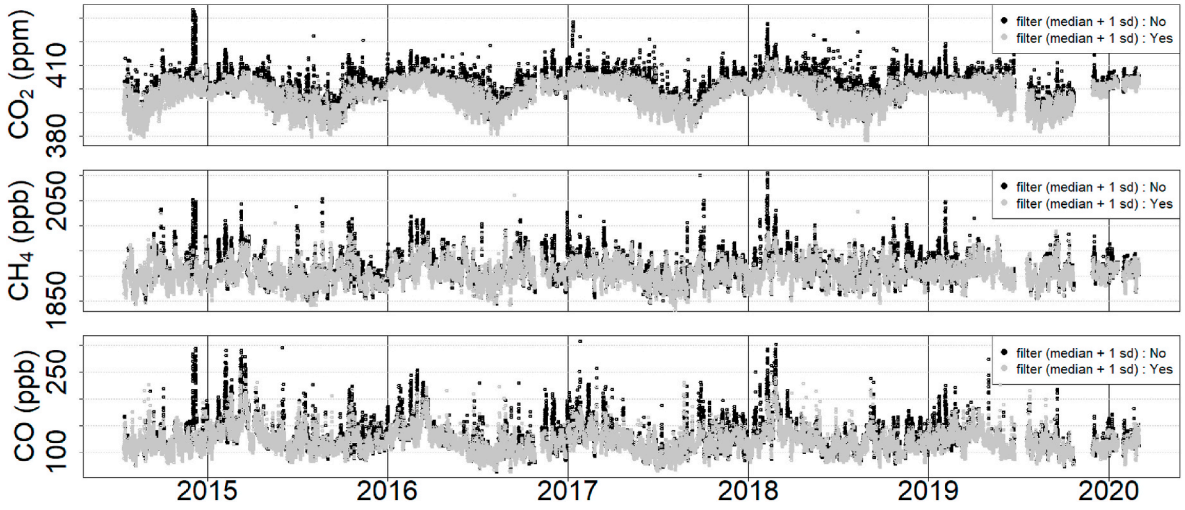

Fig. 11. (colors not required). Atmospheric CO_2 (top), CH_4 (center) and CO (bottom) timeseries measured at 100 m (AGL) before (black) and after (grey) the data filtering process described in Section 3.5.1.

associated to the southwest sector in summer from 12h00–19h00 (cf. Fig S.11) compared to an average of 1893.2 ± 21.3. Sea breezes, which are south-westerly winds (illustrated in Figs. 2 and 3), are therefore mainly associated to higher CO concentrations.

Some spikes remain on the CO timeseries even after the filtering. The high and fast variability of CO makes it difficult to find the best method to perfectly filter CO anthropogenized data points: we have tested several thresholds as illustrated on Fig. S4 and although we consider our method to be suitable to this study, more specific tests should be done in future studies to improve the data selection of CO at the OHP station.

After applying the filter, the 3 species concentrations does not show significant variability regarding wind sector and level measurements (All of the value are reported in table S.12). Whereas, the maximal difference between mean concentration regarding the wind sector are 6 ppm for CO_2 with a standard deviation close to 5 ppm regarding wind sector, the difference for CH_4 and CO are about 2 ppb and 6 ppb respectively with a standard deviation close to 20 ppb for both. CO_2 mean concentration associated with Southwest winds are close to 393.8 ppm and whereas when winds come from Northeast and East, there are close to 399.2 ppm. No difference is presented on CH_4 concentrations regarding wind sector and for CO concentration, only mean concentrations from NW sector are lower than 5 ppb compared to other which are associated with CO concentration close to 119 ppb but the standard deviation is close to 20 ppb so the difference between sector are not quite significant.

4. Conclusion

In this paper, we analysed the atmospheric in-situ data collected at OHP, one of the ICOS-France atmospheric greenhouse gases network stations located in a rural area in south-eastern France, from the 07/07/2014 to the 02/29/2020. The OHP 100 m tall tower recorded CO_2, CH_4 and CO at 10 m,50 m and 100 m (AGL) continuously, as well as meteorological parameters. The measurements and calibration process follow the ICOS specifications and are linked to the WMO-GAW international scale.

The mean annual growth rate of CO_2 (CH_4) observed at OHP was close to 2.7 ppm/year (7.8 ppb/year) and was found to be congruent with the Mauna Loa station and other ICOS stations ones, despite some interannual variations mainly driven by the variability of regional emissions, variability of natural sources and sinks and the variability of atmospheric dynamic and meteorologic conditions.

Typical seasonal variations were found at the three levels, with higher concentrations at the bottom. A seasonal amplitude of 13 ppm, 30 ppb and 45 ppb are found for CO_2, CH_4 and CO respectively. The maximal vertical gradients are 5 ppm ±0.1, 6 ppb ±0.5 and 10 ppb ±0.5, respectively, and are lower than at other ICOS rural stations (Vermeulen et al., 2011; Schmidt et al., 2014), which can be explained by the higher altitude of OHP, 650 m above the sea level (ASL). The seasonal cycle is mainly driven by the annual atmospheric dynamic, the annual vegetation cycle which represent a sink or a source for CO2 and CH_4 and finally by seasonal variability of anthropic emissions which are higher in winter due to lower temperature inducing more residential heating.

All the species show a diurnal cycle mainly driven by atmospheric boundary layer dynamics, but also by local anthropogenic sources and wind direction/speed. Strong correlations between species (R^2 between 0.67 and 0.91) have been identified in Winter, whereas no significant correlation was found during Summer congruent with Satar et al., (2016). Above 16% of the hourly data has been identified as impacted by anthropic emissions, but less than 5% are due to local short-term sources. A mean CO/CO_2 ratio of 3.72 ± 0.06 ppb/ppm was found for local sources from the observations (0.8 ± 0.2 ppb/ppm for CH_4/CO). According to the literature and local, regional, and national inventories, these ratios reflect an anthropogenic impact on the OHP station mostly from traffic and residential heating. Whereas the observed enhancements ratios and the comparison with national and literature ratio allow us to assume that 2013 ATMOSUD inventories seems overestimate CO emission from residential heating device around the OHP. For each species, more than 450 synoptics events (representing above 13% of the data), lasting a few hours to 2–3 days, have been identified 80% of these events were associated with stable synoptic meteorological conditions and low wind speeds (especially in Winter or during night-time) favourable to the accumulation of anthropogenic emissions in a shallow boundary layer. Some direct arrivals of human contaminated air masses associated with higher wind speed have been identified from the Rhône valley, the Aix Marseille Metropolis, or the Lyon/-Grenoble areas; these events represent more than a half of the recorded events seen at 100 m (AGL).

Once the data are filtered of the anthropogenic events, the OHP signal is still dependant of the wind sector. The South-West air masses show lower CO_2 concentration, by contrast with North-East and East ones which are associated with higher CO_2 mean concentration. No significant difference is seen on CH_4 signal and CO signal show lower concentration by 4–6 ppb from Northwest and West sectors compared to others wind sectors. Despite some local to regional anthropogenic influence at OHP, which impacts about 30% of hourly data, the OHP station can be used as a CO_2, CO and CH_4 background station using appropriate filters based on wind speed and concentration variability as detailed in this study, allowing the study of diurnal to pluri-annual changes, at the local, regional, and continental scales. Future work could focus on better assessing the footprint of the different cities surrounding OHP and their impacts on the site, and on characterizing the nature of the different sources contributing to this impact. Especially, adding continuous measurements of specific tracers such as NOx, black carbon, volatile organic compounds, and carbon isotopes at the OHP site would be very interesting to distinguish anthropogenic and biogenic fluxes and sources, to characterize the different anthropogenic sources, to monitor the evolution of these sources such as their enhancement ratios, and to verify independently and improve emissions inventories.

CRediT authorship contribution statement

L. Lelandais: Methodology, Formal analysis, Investigation, Writing – original draft, Writing – review & editing, Project administration. **I. Xueref-Remy:** Validation, Formal analysis, Investigation, Writing – review & editing, Supervision, Project administration. **A. Riandet:** Methodology, Writing – review & editing. **P.E. Blanc:** Resources, Data curation, Project administration. **A. Armengaud:** Funding acquisition, Resources, Data curation. **S. Oppo:** Resources, Data curation. **C. Yohia:** Resources, Data curation. **M. Ramonet:** Resources, Data curation, Funding acquisition. **M. Delmotte:** Resources, Data curation, Funding acquisition.

Declaration of competing interest

The authors declare the following financial interests/personal relationships which may be considered as potential competing interests: Edouard Bard (CEREGE), Phillipe CIAIS (LSCE), Frédérique Chevallier (LSCE). Grégoire Broquet (LSCE), François-Marie Bréon (LSCE)

Acknowledgements

We deeply thank the Conseil Regional de la Région SUD - Provence-Alpes-Côtes-d'Azur and the regional air quality monitoring agency ATMOSUD for funding the PhD grant of L. Lelandais. We are grateful to the regional OT-MED Institute at Aix-Marseille University for supporting this study within the Aix-Marseille Carbon Pilot Study (AMC Project, http://www.otmed.fr/observation-systems-and-databases/aix-marseille-carbon-pilot-study-amc). We acknowledge the ECCOREV federation, the Departmental Council of the Alpes de Haute Provence and Europe within the FEDER program for their financial support of the ICOS

OHP station. We are grateful to the ICOS-France network team for its technical and financial support of the OHP station. We acknowledge the NOAA Air Resource Laboratory (ARL) for providing the HYSPLIT Transport and dispersion model on READY website (http://www.ready.noaa.gov). We also acknowledge the IT department (SIP) from Institut OSU PYTHEAS for providing us the modeled atmospheric boundary layer height over the OHP station from the WRF-ECMWF model. The authors gratefully acknowledge ATMOSUD for providing the emissions inventory data to perform this study. We also thank the National Research Agency (ANR) for funding the PhD grant of A. Riandet.

Appendix A. Supplementary data

Supplementary data to this article can be found online at https://doi.org/10.1016/j.atmosenv.2022.119020.

References

Abshire, J., Ramanathan, A., Riris, H., Mao, J., Allan, G., Hasselbrack, W., Weaver, C., Browell, E., 2013. Airborne measurements of CO2 column concentration and range using a pulsed direct-detection IPDA lidar. Rem. Sens. 6, 443–469. https://doi.org/10.3390/rs6010443.

Ammoura, L., Xueref-Remy, I., Gros, V., Baudic, A., Bonsang, B., Petit, J.-E., Perrussel, O., Bonnaire, N., Sciare, J., Chevallier, F., 2014. Atmospheric measurements of ratios between CO $_2$ and co-emitted species from traffic : a tunnel study in the Paris megacity. Atmos. Chem. Phys. 14, 12871–12882. https://doi.org/10.5194/acp-14-12871-2014.

Ammoura, L., Xueref-Remy, I., Vogel, F., Gros, V., Baudic, A., Bonsang, B., Delmotte, M., Té, Y., Chevallier, F., 2016. Exploiting stagnant conditions to derive robust emission ratio estimates for CO $_2$, CO and volatile organic compounds in Paris. Atmos. Chem. Phys. 16, 15653–15664. https://doi.org/10.5194/acp-16-15653-2016.

Ammoura, L., Xueref-Remy, I., Vogel, F., Gros, V., Baudic, A., Bonsang, B., Delmotte, M., Té, Y., Chevallier, F., 2015. A new method for estimating emission ratios in the urban atmosphere : examples of ratios to CO $_2$, CO and volatile organic compounds in Paris. Atmos. Chem. Phys. Discuss. 15, 23587–23612. https://doi.org/10.5194/acpd-15-23587-2015.

Andreae, M.O., Merlet, P., 2001. Emission of trace gases and aerosols from biomass burning. Global Biogeochem. Cycles 15, 955–966. https://doi.org/10.1029/2000GB001382.

Andrews, G.E., Zhu, G., Li, H., Simpson, A., Wylie, J.A., Bell, M., Tate, J., 2004. The Effect of Ambient Temperature on Cold Start Urban Traffic Emissions for à Real World SI Car. In: Presented at the 2004 Powertrain & Fluid Systems Conference & Exhibition. https://doi.org/10.4271/2004-01-2903, 2004-01–2903.

Arias-Ortiz, A., Serrano, O., Masqué, P., Lavery, P.S., Mueller, U., Kendrick, G.A., Rozaimi, M., Esteban, A., Fourqurean, J.W., Marbà, N., Mateo, M.A., Murray, K., Rule, M.J., Duarte, C.M., 2018. A marine heatwave drives massive losses from the world's largest seagrass carbon stocks. Nat. Clim. Change 8, 338–344. https://doi.org/10.1038/s41558-018-0096-y.

Bakas, N.A., Fotiadi, A., Kariofillidi, S., 2020. Climatology of the boundary layer height and of the wind field over Greece. Atmosphere 11, 910. https://doi.org/10.3390/atmos11090910.

Bakwin, P.S., Tans, P.P., Hurst, D.F., Zhao, C., 1998. Measurements of Carbon Dioxide on Very Tall Towers : Results of the NOAA/CMDL Program 15.

Bares, R., Lin, J.C., Hoch, S.W., Baasandorj, M., Mendoza, D.L., Fasoli, B., Mitchell, L., Catharine, D., Stephens, B.B., 2018. The wintertime covariation of CO $_2$ and criteria pollutants in an urban valley of the western United States. J. Geophys. Res. Atmos. 123, 2684–2703. https://doi.org/10.1002/2017JD027917.

Bastin, S., Drobinski, P., 2006. Sea-breeze-induced mass transport over complex terrain in south-eastern France: A case-study. Q. J. R. Meteorol. Soc. https://doi.org/10.1256/qj.04.111.

Beck, H.E., Zimmermann, N.E., McVicar, T.R., Vergopolan, N., Berg, A., Wood, E.F., 2018. Present and future Köppen-Geiger climate classification maps at 1-km resolution. Sci. Data 5, 180214. https://doi.org/10.1038/sdata.2018.214.

Belviso, S., Reiter, I., Loubet, B., Gros, V., Lathière, J., Montagne, D., Delmotte, M., Ramonet, M., Kalogridis, C., Lebegue, B., Bonnaire, N., Kazan, V., Gauquelin, T., Fernandez, C., Genty, B., 2016. A top-down approach of surface carbonyl sulfide exchange by a Mediterranean oak forest ecosystem in southern France. Atmos. Chem. Phys. 16.

Bergamaschi, P., et al., 2018. Inverse modelling of European CH4 emissions during 2006–2012 using different inverse models and reassessed atmospheric observations. Atmos. Chem. Phys. https://doi.org/10.5194/acp-18-901-2018.

Betts, R.A., Jones, C.D., Knight, Jeff.R., Keeling, Ralph.F., Kennedy, John.J., Wiltshire, A. J., Andrew, R.M., Aragão, L.E.O.C., 2018. A successful prediction of the record CO $_2$ rise associated with the 2015/2016 El Niño. Phil. Trans. R. Soc. B 373, 20170301. https://doi.org/10.1098/rstb.2017.0301.

Boothroyd, I.M., Almond, S., Worrall, F., Davies, R.K., Davies, R.J., 2018. Assessing fugitive emissions of CH4 from high-pressure gas pipelines in the UK. Sci. Total Environ. 631–632, 1638–1648. https://doi.org/10.1016/j.scitotenv.2018.02.240.

Broquet, G., Chevallier, F., Bréon, F.-M., Kadygrov, N., Alemanno, M., Apadula, F., Hammer, S., Haszpra, L., Meinhardt, F., Morguí, J.A., 2013. Regional inversion of CO 2 ecosystem fluxes from atmospheric measurements : reliability of the uncertainty estimates. Atmos. Chem. Phys. 13, 9039–9056.

Buchholz, R.R., Paton-Walsh, C., Griffith, D.W.T., Kubistin, D., Caldow, C., Fisher, J.A., Deutscher, N.M., Kettlewell, G., Riggenbach, M., Macatangay, R., Krummel, P.B., Langenfelds, R.L., 2016. Source and meteorological influences on air quality (CO, CH4 & CO2) at a Southern Hemisphere urban site. Atmos. Environ. 126, 274–289. https://doi.org/10.1016/j.atmosenv.2015.11.041.

Carslaw, D., et al., 2012. openair — An R package for air quality data analysis. Elsevier. https://doi.org/10.1016/j.envsoft.2011.09.008.

Chevallier, F., Ciais, P., Conway, T.J., Aalto, T., Anderson, B.E., Bousquet, P., Brunke, E. G., Ciattaglia, L., Esaki, Y., Fröhlich, M., 2010. CO2 surface fluxes at grid point scale estimated from a global 21 year reanalysis of atmospheric measurements. J. Geophys. Res. Atmos. 115.

Conil, S., Helle, J., Langrene, L., Laurent, O., Ramonet, M., 2019. Continuous atmospheric CO&lt ; sub&gt ;2</sub&gt ; CH&lt ; sub&gt ;4</sub&gt ; and CO measurements at the OPE station in France from 2011 to 2018 (preprint). Gases/In Situ Measurement/Instruments and Platforms. https://doi.org/10.5194/amt-2019-128.

Curcoll, R., Camarero, L., Bacardit, M., Àgueda, A., Grossi, C., Gacia, E., Font, A., Morguí, J.-A., 2019. Atmospheric carbon dioxide variability at Aigüestortes, central Pyrenees, Spain. Reg. Environ. Change 19, 313–324. https://doi.org/10.1007/s10113-018-1443-2.

Delbarre, H., Augustin, P., Saïd, F., Campistron, B., Bénech, B., Lohou, F., Puygrenier, V., Moppert, C., Cousin, F., Fréville, P., Fréjafon, E., 2005. Ground-based remote sensing observation of the complex behaviour of the Marseille boundary layer during ESCOMPTE. Atmos. Res. 74, 403–433. https://doi.org/10.1016/j.atmosres.2004.04.007.

Doukalianou, F., Radoglou, K., Agnelli, A.E., Kitikidou, K., Milios, E., Orfanoudakis, M., Lagomarsino, A., 2019. Annual greenhouse-gas emissions from forest soil of a peri-urban conifer forest in Greece under different thinning intensities and their climate-change mitigation potential. For. Sci. 65, 387–400. https://doi.org/10.1093/forsci/fxy069.

Draxler, R., et al., 1997. Descripition of the Hysplit_4 modeling system. NOAA Tech. Memo. ERL ARL-224.

Drobinski, P., Bastin, S., Dabas, A., Delville, P., Reitebuch, O., 2006. Variability of three-dimensional sea breeze structure in southern France : observations and evaluation of empirical scaling laws. Ann. Geophys. 24, 1783–1799. https://doi.org/10.5194/angeo-24-1783-2006.

Drobinski, P., Bastin, S., Guenard, V., Caccia, J.-L., Dabas, A.M., Delville, P., Protat, A., Reitebuch, O., Werner, C., 2005. Summer mistral at the exit of the Rhône valley. Q. J. R. Meteorol. Soc. 131, 353–375. https://doi.org/10.1256/qj.04.63.

Dlugokencky, E.D., Tans, P., 2020. Recent Global CO2. www.esrl.noaa.gov/gmd/ccgg/trends/.

El Yazidi, A., Ramonet, M., Ciais, P., Broquet, G., Pison, I., Abbaris, A., Brunner, D., Conil, S., Delmotte, M., Gheusi, F., Guerin, F., Hazan, L., Kachroudi, N., Kouvarakis, G., Mihalopoulos, N., Rivier, L., Serça, D., 2018. Identification of spikes associated with local sources in continuous time series of atmospheric CO, CO $_2$ and CH $_4$. Atmos. Meas. Tech. 11, 1599–1614. https://doi.org/10.5194/amt-11-1599-2018.

Fang, S., Lin, D., Tian, Y., Hong, S., 2016. Thinning intensity affects soil-atmosphere fluxes of greenhouse gases and soil nitrogen mineralization in a lowland poplar plantation. Forests 7, 141. https://doi.org/10.3390/f7070141.

Fernández-Duque, B., Pérez, I.A., Sánchez, M.L., García, M.Á., Pardo, N., 2017. Temporal Patterns of CO 2 and CH 4 in a Rural Area in Northern Spain Described by a Harmonic Equation over 2010–2016. Science of the Total Environment, pp. 1–9. https://doi.org/10.1016/j.scitotenv.2017.03.132, 593–594.

Fujitani, T., 1986. Seasonal variation of the structure of the atmospheric boundary layer over a Suburban area. Atmos. Environ. 20, 1867–1876. https://doi.org/10.1016/0004-6981(86)90327-6, 1967.

Gaudry, A., Monfray, P., Polian, G., Lambert, G., 1987. The 1982-1983 El Niño : a 6 billions ton CO $_2$ release. Tellus B 39B, 209. https://doi.org/10.1111/j.1600-0889.1987.tb00283.x. –213.

Geels, C., Gloor, M., Ciais, P., Bousquet, P., Peylin, P., Vermeulen, A.T., Dargaville, R., Aalto, T., Brandt, J., Christensen, J.H., Frohn, L.M., Haszpra, L., Karstens, U., Rödenbeck, C., Ramonet, M., Carboni, G., Santaguida, R., 2007. Comparing atmospheric transport models for future regional inversions over Europe &ndash ; Part 1 : mapping the atmospheric CO_2 signals. Atmos. Chem. Phys. 7, 3461–3479. https://doi.org/10.5194/acp-7-3461-2007.

Gerdol, R., Bragazza, L., Brancaleoni, L., 2008. Heatwave 2003 : high summer temperature, rather than experimental fertilization, affects vegetation and CO $_2$ exchange in an alpine bog. New Phytol. 179, 142–154. https://doi.org/10.1111/j.1469-8137.2008.02429.x.

Gu, J., Zhang, Y., Yang, N., Wang, R., School of Hydrology and water Resources, Nanjing University of Information Science and technology, Nanjing 210044, China, & State Oceanic Administration Key Laboratory for Polar Science, Polar Research Institute of China, Shanghai 200136, China, 2020. Diurnal variability of the planetary boundary layer height estimated from radiosonde data. Earth Planet. Phys. 4 (5), 1–14. https://doi.org/10.26464/epp2020042.

Hall, B.D., Crotwell, A.M., Kitzis, D.R., Mefford, T., Miller, B.R., Schibig, M.F., Tans, P.P., 2020. Revision of the WMO/GAW CO&lt ; sub&gt ;2</sub&gt ; Calibration Scale (preprint). Gases/Lab. Meas./Validat. Intercompa. https://doi.org/10.5194/amt-2020-408.

Haszpra, L., Barcza, Z., Bakwin, P.S., Berger, B.W., Davis, K.J., Weidinger, T., 2001. Measuring system for the long-term monitoring of biosphere/atmosphere exchange of carbon dioxide. J. Geophys. Res. Atmos. 106, 3057–3069.

Hausmann, P., Sussmann, R., Smale, D., 2016. Contribution of oil and natural gas production to renewed increase in atmospheric methane (2007–2014): top–down estimate from ethane and methane column observations. Atmos. Chem. Phys. 16, 3227–3244. https://doi.org/10.5194/acp-16-3227-2016.

Hazan, L., Tarniewicz, J., Ramonet, M., Laurent, O., Abbaris, A., 2016. Automatic processing of atmospheric CO $_2$ and CH $_4$ mole fractions at the ICOS Atmosphere Thematic Centre. Atmos. Meas. Tech. 9, 4719–4736. https://doi.org/10.5194/amt-9-4719-2016.

Houweling, S., Baker, D., Basu, S., Boesch, H., Butz, A., Chevallier, F., Deng, F., Dlugokencky, E.J., Feng, L., Ganshin, A., Hasekamp, O., Jones, D., Maksyutov, S., Marshall, J., Oda, T., O'Dell, C.W., Oshchepkov, S., Palmer, P.I., Peylin, P., Poussi, Z., Reum, F., Takagi, H., Yoshida, Y., Zhuravlev, R., 2015. An intercomparison of inverse models for estimating sources and sinks of CO $_2$ using GOSAT measurements : GOSAT inversion inter-comparison. J. Geophys. Res. Atmos. 120, 5253–5266. https://doi.org/10.1002/2014JD022962.

Hu, C., et al., 2018. Top-Down Constraints on Anthropogenic CO2 Emissions Within an Agricultural-Urban Landscape. J. Geophys. Res. Atmos. https://doi.org/10.1029/2017JD027881. In press.

Idso, S.B., Idso, C.D., Balling, R.C., 2002. Seasonal and diurnal variations of near-surface atmospheric CO2 concentration within a residential sector of the urban CO2 dome of Phoenix, AZ, USA. Atmos. Environ. 36, 1655–1660. https://doi.org/10.1016/S1352-2310(02)00159-0.

Intergovernmental Panel on Climate Change, 2014. Climate Change 2014 Mitigation of Climate Change : Working Group III Contribution to the Fifth Assessment Report of the Intergovernmental Panel on Climate Change. Cambridge University Press, Cambridge. https://doi.org/10.1017/CBO9781107415416.

Jiang, Q., Smith, R.B., Doyle, J., 2003. The nature of the mistral : observations and modelling of two MAP events. Q. J. R. Meteorol. Soc. 129, 857–875. https://doi.org/10.1256/qj.02.21.

Keeling, C.D., 1960. The concentration and isotopic abundances of carbon dioxide in the atmosphere. Tellus 12, 200–203. https://doi.org/10.1111/j.2153-3490.1960.tb01300.x.

Kirschke, S., Bousquet, P., Ciais, P., Saunois, M., Canadell, J.G., Dlugokencky, E.J., Bergamaschi, P., Bergmann, D., Blake, D.R., Bruhwiler, L., Cameron-Smith, P., Castaldi, S., Chevallier, F., Feng, L., Fraser, A., Heimann, M., Hodson, E.L., Houweling, S., Josse, B., Fraser, P.J., Krummel, P.B., Lamarque, J.-F., Langenfelds, R. L., Le Quéré, C., Naik, V., O'Doherty, S., Palmer, P.I., Pison, I., Plummer, D., Poulter, B., Prinn, R.G., Rigby, M., Ringeval, B., Santini, M., Schmidt, M., Shindell, D. T., Simpson, I.J., Spahni, R., Steele, L.P., Strode, S.A., Sudo, K., Szopa, S., van der Werf, G.R., Voulgarakis, A., van Weele, M., Weiss, R.F., Williams, J.E., Zeng, G., 2013. Three decades of global methane sources and sinks. Nat. Geosci. 6, 813–823. https://doi.org/10.1038/ngeo1955.

Koffi, E.N., Bergamaschi, P., Karstens, U., Krol, M., Segers, A., Schmidt, M., Levin, I., Vermeulen, A.T., Fisher, R.E., Kazan, V., Klein Baltink, H., Lowry, D., Manca, G., Meijer, H.A.J., Moncrieff, J., Pal, S., Ramonet, M., Scheeren, H.A., 2016. Evaluation of the boundary layer dynamics of the TM5 model (preprint). Climate and Earth System Modeling. https://doi.org/10.5194/gmd-Clim. Earth Syst. Model.2016-48.

Kort, E.A., Frankenberg, C., Miller, C.E., Oda, T., 2012. Space-based observations of megacity carbon dioxide : space-based observations OF megacity CO $_2$. Geophys. Res. Lett. 39 https://doi.org/10.1029/2012GL052738 n/a-n/a.

Kountouris, P., Gerbig, C., Rödenbeck, C., Karstens, U., Koch, T.F., Heimann, M., 2018. Atmospheric CO2 inversions on the mesoscale using data-driven prior uncertainties : quantification of the European terrestrial CO2 fluxes. Atmos. Chem. Phys. 18, 3047–3064.

Laurent, O., 2017. ICOS Atmospheric Station Specifications. ICOS technical report (publicly available on. https://icos-tc.lsce.ipsl.fr/doc_public.

Lin, X., Indira, N.K., Ramonet, M., Delmotte, M., Ciais, P., Bhatt, B.C., Reddy, M.V., Angchuk, D., Balakrishnan, S., Jorphail, S., Dorjai, T., Mahey, T.T., Patnaik, S., Begum, M., Brenninkmeijer, C., Durairaj, S., Kirubagaran, R., Schmidt, M., Swathi, P. S., Vinithkumar, N.V., Yver Kwok, C., Gaur, V.K., 2015. Long-lived atmospheric trace gases measurements in flask samples from three stations in India. Atmos. Chem. Phys. 15, 9819–9849. https://doi.org/10.5194/acp-15-9819-2015.

Liu, C., Huang, J., Wang, Y., Tao, X., Hu, C., Deng, L., Xu, J., Xiao, H.-W., Luo, L., Xiao, H.-Y., Xiao, W., 2020. Vertical distribution of PM2.5 and interactions with the atmospheric boundary layer during the development stage of a heavy haze pollution event. Sci. Total Environ. 704, 135329. https://doi.org/10.1016/j.scitotenv.2019.135329.

Liu, H.Z., Feng, J.W., Järvi, L., Vesala, T., 2012. Four-year (2006–2009) eddy covariance measurements of CO_2 flux over an urban area in Beijing. Atmos. Chem. Phys. 12, 7881–7892. https://doi.org/10.5194/acp-12-7881-2012.

Liu, S., Liang, X.-Z., 2010. Observed diurnal cycle climatology of planetary boundary layer height. J. Clim. 23, 5790–5809. https://doi.org/10.1175/2010JCLI3552.1.

Lopez, M., Schmidt, M., Delmotte, M., Colomb, A., Gros, V., Janssen, C., Lehman, S.J., Mondelain, D., Perrussel, O., Ramonet, M., Xueref-Remy, I., Bousquet, P., 2013. CO, NO $_x$ and ^{13} CO $_2$ as tracers for fossil fuel CO $_2$: results from a pilot study in Paris during winter 2010. Atmos. Chem. Phys. 13, 7343–7358. https://doi.org/10.5194/acp-13-7343-2013.

Lowry, D., Lanoisellé, M.E., Fisher, R.E., Martin, M., Fowler, C.M.R., France, J.L., Hernández-Paniagua, I.Y., Novelli, P.C., Sriskantharajah, S., O'Brien, P., Rata, N.D., Holmes, C.W., Fleming, Z.L., Clemitshaw, K.C., Zazzeri, G., Pommier, M., McLinden, C.A., Nisbet, E.G., 2016. Marked long-term decline in ambient CO mixing ratio in SE England, 1997–2014 : evidence of policy success in improving air quality. Sci. Rep. 6, 25661. https://doi.org/10.1038/srep25661.

McKain, K., Wofsy, S.C., Nehrkorn, T., Eluszkiewicz, J., Ehleringer, J.R., Stephens, B.B., 2012. Assessment of ground-based atmospheric observations for verification of greenhouse gas emissions from an urban region. Proc. Natl. Acad. Sci. Unit. States Am. 109, 8423–8428. https://doi.org/10.1073/pnas.1116645109.

Medeiros, B., Hall, A., Stevens, B., 2005. What controls the mean depth of the PBL. J. Clim. 18, 3157–3172. https://doi.org/10.1175/JCLI3417.1.

Miller, J.B., Lehman, S.J., Verhulst, K.R., Miller, C.E., Duren, R.M., Yadav, V., Newman, S., Sloop, C.D., 2020. Large and seasonally varying biospheric CO $_2$ fluxes in the Los Angeles megacity revealed by atmospheric radiocarbon. Proc. Natl. Acad. Sci. U.S.A. 117, 26681–26687. https://doi.org/10.1073/pnas.2005253117.

Mühle, J., Brenninkmeijer, C.A.M., Rhee, T.S., Slemr, F., Oram, D.E., Penkett, S.A., Zahn, A., 2002. Biomass burning and fossil fuel signatures in the upper troposphere observed during a CARIBIC flight from Namibia to Germany : biomass burning and fossil fuel signatures. Geophys. Res. Lett. 29 https://doi.org/10.1029/2002GL015764, 16-1-16–4.

Nasrallah, H.A., Balling Jr., R.C., Mohammed Madi, S., Al-Ansari, L., 2003. Temporal variations in atmospheric CO2 concentrations in Kuwait City, Kuwait with comparisons to Phoenix, Arizona, USA. Environ. Pollut. 121, 301–305. https://doi.org/10.1016/S0269-7491(02)00221-X.

Patra, P.K., Maksyutov, S., Nakazawa, T., 2005. Analysis of atmospheric CO $_2$ growth rates at Mauna Loa using CO $_2$ fluxes derived from an inverse model. Tellus B 57, 357–365. https://doi.org/10.3402/tellusb.v57i5.16560.

Popa, M.E., Gloor, M., Manning, A.C., Jordan, A., Schultz, U., Haensel, F., Seifert, T., Heimann, M., 2010. Measurements of greenhouse gases and related tracers at Bialystok tall tower station in Poland. Atmos. Meas. Tech. 21.

Popa, M.E., Vollmer, M.K., Jordan, A., Brand, W.A., Pathirana, S.L., Rothe, M., Röckmann, T., 2014. Vehicle emissions of greenhouse gases and related tracers from a tunnel study : CO : CO $_2$, N $_2$ O : CO $_2$, CH $_4$: CO $_2$, O $_2$: CO $_2$ ratios, and the stable isotopes ^{13} C and ^{18} O in CO $_2$ and CO. Atmos. Chem. Phys. 14, 2105–2123. https://doi.org/10.5194/acp-14-2105-2014.

Ramonet, M., et al., 2017. A recent build-up of atmospheric CO2 over Europe. Part 1: observed signals and possible explanations. Tellus B: Chem. Phys. Meteorol. https://doi.org/10.1111/j.1600-0889.2009.00442.x.

Ramonet, M., Ciais, P., Apadula, F., Bartyzel, J., Bastos, A., Bergamaschi, P., Blanc, P.E., Brunner, D., Caracciolo di Torchiarolo, L., Calzolari, F., Chen, H., Chmura, L., Colomb, A., Conil, S., Cristofanelli, P., Cuevas, E., Curcoll, R., Delmotte, M., di Sarra, A., Emmenegger, L., Forster, G., Frumau, A., Gerbig, C., Gheusi, F., Hammer, S., Haszpra, L., Hatakka, J., Hazan, L., Heliasz, M., Henne, S., Hensen, A., Hermansen, O., Keronen, P., Kivi, R., Komínková, K., Kubistin, D., Laurent, O., Laurila, T., Lavric, J.V., Lehner, I., Lehtinen, K.E.J., Leskinen, A., Leuenberger, M., Levin, I., Lindauer, M., Lopez, M., Myhre, C.L., Mammarella, I., Manca, G., Manning, A., Marek, M.V., Marklund, P., Martin, D., Meinhardt, F., Mihalopoulos, N., Mölder, M., Morgui, J.A., Necki, J., O'Doherty, S., O'Dowd, C., Ottosson, M., Philippon, C., Piacentino, S., Pichon, J.M., Plass-Duelmer, C., Resovsky, A., Rivier, L., Rodó, X., Sha, M.K., Scheeren, H.A., Sferlazzo, D., Spain, T. G., Stanley, K.M., Steinbacher, M., Trisolino, P., Vermeulen, A., Vítková, G., Weyrauch, D., Xueref-Remy, I., Yala, K., Yver Kwok, C., 2020. The fingerprint of the summer 2018 drought in Europe on ground-based atmospheric CO $_2$ measurements. Phil. Trans. R. Soc. B 375, 20190513. https://doi.org/10.1098/rstb.2019.0513.

Rayner, P.J., Raupach, M.R., Paget, M., Peylin, P., Koffi, E., 2010. A new global gridded data set of CO $_2$ emissions from fossil fuel combustion : Methodology and evaluation. J. Geophys. Res. 115, D19306. https://doi.org/10.1029/2009JD013439.

Rigby, M., Montzka, S.A., Prinn, R.G., White, J.W.C., Young, D., O'Doherty, S., Lunt, M. F., Ganesan, A.L., Manning, A.J., Simmonds, P.G., Salameh, P.K., Harth, C.M., Mühle, J., Weiss, R.F., Fraser, P.J., Steele, L.P., Krummel, P.B., McCulloch, A., Park, S., 2017. Role of atmospheric oxidation in recent methane growth. Proc. Natl. Acad. Sci. U.S.A. 114, 5373–5377. https://doi.org/10.1073/pnas.1616426114.

Rödenbeck, C., Zaehle, S., Keeling, R., Heimann, M., 2020. The European carbon cycle response to heat and drought as seen from atmospheric CO $_2$ data for 1999–2018. Phil. Trans. R. Soc. B 375, 20190506. https://doi.org/10.1098/rstb.2019.0506.

Roustant, O., n.d. INTRODUCTION AUX SÉRIES CHRONOLOGIQUES 51.

Saeki, T., Maksyutov, S., Sasakawa, M., Machida, T., Arshinov, M., Tans, P., Conway, T. J., Saito, M., Valsala, V., Oda, T., Andres, R.J., Belikov, D., 2013. Carbon flux estimation for Siberia by inverse modeling constrained by aircraft and tower CO $_2$ measurements : carbon flux estimation using siberian CO $_2$ measurements. J. Geophys. Res. Atmos. 118, 1100–1122. https://doi.org/10.1002/jgrd.50127.

Satar, E., Berhanu, T.A., Brunner, D., Henne, S., Leuenberger, M., 2016. Continuous CO2/CH4/CO measurements (2012–2014) at Beromünster tall tower station in Switzerland. Biogeosciences 13, 2623–2635. https://doi.org/10.5194/bg-13-2623-2016.

Schaefer, H., et al., 2016. A 21st century shift from fossil-fuel to biogenic methane emissions indicated by 13CH4. Science 352, 80–84.

Schmidt, M., Graul, R., Sartorius, H., Levin, I., 2003. The Schauinsland CO2 record : 30 years of continental observations and their implications for the variability of the European CO2 budget. J. Geophys. Res. Atmos. 108.

Schmidt, M., Lopez, M., Yver Kwok, C., Messager, C., Ramonet, M., Wastine, B., Vuillemin, C., Truong, F., Gal, B., Parmentier, E., Cloué, O., Ciais, P., 2014. High-precision quasi-continuous atmospheric greenhouse gas measurements at Trainou tower (Orléans forest, France). Atmos. Meas. Tech. 7, 2283–2296. https://doi.org/10.5194/amt-7-2283-2014.

Schultz, M.G., Akimoto, H., Bottenheim, J., Buchmann, B., Galbally, I.E., Gilge, S., Helmig, D., Koide, H., Lewis, A.C., Novelli, P.C., Plass-Dülmer, C., Ryerson, T.B., Steinbacher, M., Steinbrecher, R., Tarasova, O., Tørseth, K., Thouret, V., Zellweger, C., 2015. The Global Atmosphere Watch reactive gases measurement network. Elem. Sci. Anth. 3, 000067 https://doi.org/10.12952/journal.elementa.000067.

Sen, P.K., 2021. Estimates of the Regression Coefficient Based on Kendall's Tau 12.

Skamarock, W.C., 2004. Evaluating mesoscale NWP models using kinetic energy spectra. Mon. Weather Rev. 132, 3019–3032.
Smith, N.E., Kooijmans, L.M.J., Koren, G., van Schaik, E., van der Woude, A.M., Wanders, N., Ramonet, M., Xueref-Remy, I., Siebicke, L., Manca, G., Brümmer, C., Baker, I.T., Haynes, K.D., Luijkx, I.T., Peters, W., 2020. Spring enhancement and summer reduction in carbon uptake during the 2018 drought in northwestern Europe. Phil. Trans. R. Soc. B 375, 20190509. https://doi.org/10.1098/rstb.2019.0509.
Stanley, K.M., Grant, A., Doherty, S., Young, D., Manning, A.J., Stavert, A.R., Spain, T.G., Salameh, P.K., Harth, C.M., Simmonds, P.G., Sturges, W.T., Oram, D.E., Derwent, R. G., 2018. Greenhouse gas measurements from a UK network of tall towers : technical description and first results. Atmos. Meas. Tech. 11, 1437–1458. https://doi.org/10.5194/amt-11-1437-2018. O& apos.
Stavert, A.R., Doherty, S., Stanley, K., Young, D., Manning, A.J., Lunt, M.F., Rennick, C., Arnold, T., 2019. UK greenhouse gas measurements at two new tall towers for aiding emissions verification. Atmos. Meas. Tech. 12, 4495–4518. https://doi.org/10.5194/amt-12-4495-2019. O& apos.
Turner, A.J., Frankenberg, C., Wennberg, P.O., Jacob, D.J., 2017. Ambiguity in the causes for decadal trends in atmospheric methane and hydroxyl. Proc. Natl. Acad. Sci. U.S.A. 114, 5367–5372. https://doi.org/10.1073/pnas.1616020114.
Turner, A.J., Frankenberg, C., Kort, E.A., 2019. Interpreting contemporary trends in atmospheric methane. Proc. Natl. Acad. Sci. U.S.A. 116, 2805–2813. https://doi.org/10.1073/pnas.1814297116.
United Nation Climate Change, 2015. Paris Agreements. In: https://unfccc.int/process-and meetings/the-paris-agreement/the-paris-agreement/key-aspects-of-the-paris-agreement.
Uglietti, C., Leuenberger, M., Brunner, D., 2011. Large-scale European source and flow patterns retrieved from back-trajectory interpretations of CO&lt ; sub&gt ;2</ sub&gt ; at the high alpine research station Jungfraujoch. Atmos. Chem. Phys. Discuss. 11, 813–857. https://doi.org/10.5194/acpd-11-813-2011.
van Oldenborgh, G.J., Philip, S., Kew, S., Otto, F., Haustein, K., Vautard, R., Boucher, O., Soubeyroux, J.-M., Ribes, A., Robin, Y., Seneviratne, S.I., Vogel, M.M., Stott, P., van Aalst, M., n.d. Human Contribution to the Record-Breaking June 2019 Heat Wave in France 32.
Vautard, R., van Aalst, M., Boucher, O., Drouin, A., Haustein, K., Kreienkamp, F., van Oldenborgh, G.J., Otto, F.E.L., Ribes, A., Robin, Y., Schneider, M., Soubeyroux, J.-M., Stott, P., Seneviratne, S.I., Vogel, M.M., Wehner, M., 2020. Human contribution to the record-breaking June and July 2019 heatwaves in western Europe. Environ. Res. Lett. 15, 094077 https://doi.org/10.1088/1748-9326/aba3d4.
Vermeulen, A.T., Hensen, A., Popa, M.E., van den Bulk, W.C.M., Jongejan, P.A.C., 2011. Greenhouse gas observations from Cabauw tall tower (1992–2010). Atmos. Meas. Tech. 4, 617–644. https://doi.org/10.5194/amt-4-617-2011.
Vogel, F., Hamme, S., Steinhof, A., Kromer, B., Levin, I., 2010. Implication of weekly and diurnal ^{14} C calibration on hourly estimates of CO-based fossil fuel CO $_2$ ata moderately polluted site in southwestern Germany. Tellus B 62, 512–520. https://doi.org/10.1111/j.1600-0889.2010.00477.x.
Wang, W., Ciais, P., Nemani, R.R., Canadell, J.G., Piao, S., Sitch, S., White, M.A., Hashimoto, H., Milesi, C., Myneni, R.B., 2013. Variations in atmospheric CO2 growth rates coupled with tropical temperature. Proc. Natl. Acad. Sci. Unit. States Am. 110, 13061–13066. https://doi.org/10.1073/pnas.1219683110.
Ward, H.C., et al., 2015. Effects of urban density on carbon dioxide exchanges: Observations of dense urban, suburban and woodland areas of southern England. Elsevier. https://doi.org/10.1016/j.envpol.2014.12.031.
Wu, D., Zhao, X., Liang, S., Zhou, T., Huang, K., Tang, B., Zhao, W., 2015. Time-lag effects of global vegetation responses to climate change. Global Change Biol. 21, 3520–3531. https://doi.org/10.1111/gcb.12945.
Xia, L., Zhang, G., Liu, L., Li, B., Zhan, M., Kong, P., Wang, H., 2020. Atmospheric CO2 and CO at Jingdezhen station in central China : understanding the regional transport and combustion efficiency. Atmos. Environ. 222, 117104. https://doi.org/10.1016/j.atmosenv.2019.117104.
Xiang, Y., Zhang, T., Liu, J., Lv, L., Dong, Y., Chen, Z., 2019. Atmosphere boundary layer height and its effect on air pollutants in Beijing during winter heavy pollution. Atmos. Res. 215, 305–316. https://doi.org/10.1016/j.atmosres.2018.09.014.
Xueref-Remy, I., Dieudonné, E., Vuillemin, C., Lopez, M., Lac, C., Schmidt, M., Delmotte, M., Chevallier, F., Ravetta, F., Perrussel, O., Ciais, P., Bréon, F.-M., Broquet, G., Ramonet, M., Spain, T.G., Ampe, C., 2018. Diurnal, synoptic and seasonal variability of atmospheric CO $_2$ in the Paris megacity area. Atmos. Chem. Phys. 18, 3335–3362. https://doi.org/10.5194/acp-18-3335-2018.
Xueref-Remy, I., Messager, C., Filippi, D., Pastel, M., Nedelec, P., Ramonet, M., Paris, J. D., Ciais, P., 2011. Variability and budget of CO $_2$ in Europe : analysis of the CAATER airborne campaigns – Part 1 : observed variability. Atmos. Chem. Phys. 11, 5655–5672. https://doi.org/10.5194/acp-11-5655-2011.
Xueref-Remy, I., Zazzeri, G., Bréon, F.M., Vogel, F., Ciais, P., Lowry, D., Nisbet, E.G., 2020. Anthropogenic methane plume detection from point sources in the Paris megacity area and characterization of their δ13C signature. Atmos. Environ. 222, 117055. https://doi.org/10.1016/j.atmosenv.2019.117055.
Ye, X., Lauvaux, T., Kort, E.A., Oda, T., Feng, S., Lin, J.C., Yang, E.G., Wu, D., 2020. Constraining fossil fuel CO $_2$ emissions from urban area using OCO-2 observations of total column CO $_2$. J. Geophys. Res. Atmos. 125 https://doi.org/10.1029/2019JD030528.
Yver Kwok, C., Laurent, O., Guemri, A., Philippon, C., Wastine, B., Rella, C.W., Vuillemin, C., Truong, F., Delmotte, M., Kazan, V., Darding, M., Lebègue, B., Kaiser, C., Xueref-Rémy, I., Ramonet, M., 2015. Comprehensive laboratory and field testing of cavity ring-down spectroscopy analyzers measuring H $_2$ O, CO $_2$, CH $_4$ and CO. Atmos. Meas. Tech. 8, 3867–3892. https://doi.org/10.5194/amt-8-3867-2015.

Further reading

Beck, E.-G., 2008. 50 Years of Continuous measurement of CO_2 on mauna loa. Energy Environ. 19.